CARDIFF UNIVERSITY
PRIFYSGOL CAERDYDD

ORCA – Online Research @ Cardiff

This is an Open Access document downloaded from ORCA, Cardiff University's institutional repository:https://orca.cardiff.ac.uk/id/eprint/146855/

This is the author's version of a work that was submitted to / accepted for publication.

Citation for final published version:

Stanton, Stephen A., Du, Jonathan J., Lai, Felcia, Stanton, Gyte, Hawkins, Bryson A., Ong, Jennifer A., Groundwater, Paul W., Platts, James A. and Hibbs, David E. 2021. Understanding hygroscopicity of theophylline via a novel cocrystal polymorph: a charge density study. The Journal of Physical Chemistry A 125 (45) , 9736–9756. 10.1021/acs.jpca.0c09536

Publishers page: http://dx.doi.org/10.1021/acs.jpca.0c09536

Please note:
Changes made as a result of publishing processes such as copy-editing, formatting and page numbers may not be reflected in this version. For the definitive version of this publication, please refer to the published source. You are advised to consult the publisher's version if you wish to cite this paper.

This version is being made available in accordance with publisher policies. See http://orca.cf.ac.uk/policies.html for usage policies. Copyright and moral rights for publications made available in ORCA are retained by the copyright holders.

Understanding Hygroscopicity of Theophylline *via* a Novel Co-Crystal Polymorph: A Charge Density Study

Stephen A. Stanton,[1] Jonathan J. Du,[1,3] Felcia Lai,[1] Gyte Stanton, [1] Bryson A. Hawkins,[1] Jennifer A. Ong,[1] Paul W. Groundwater,[1] James A. Platts,[2] and David E. Hibbs[1]*

[1]*Sydney School of Pharmacy, Faculty of Medicine and Health, The University of Sydney, NSW 2006 Australia*

[2]*School of Chemistry, Cardiff University, Cardiff, CF10 3AT, UK*

[3]*Current Address: Department of Biochemistry, School of Medicine, Emory University, Atlanta, Georgia, USA*

**Corresponding author: David E. Hibbs, david.hibbs@sydney.edu.au*

Abstract

The charge density distribution in a novel co-crystal (1) complex of 1,3-dimethylxanthine (theophylline) and propanedioic acid (malonic acid) has been determined. The molecules crystallise in the triclinic, centrosymmetric space group $P\bar{1}$, with four independent molecules (Z=4) in the asymmetric unit [two molecules each of theophylline and malonic acid. Theophylline has a notably high hygroscopic nature and numerous co-crystals have shown a significant improvement in stability to humidity. A charge density study of the novel polymorph has identified interesting theoretical results correlating the stability enhancement of theophylline via co-crystallisation. Topological analysis of the electron density highlighted key differences (up to 17.8) in Laplacian ($\nabla^2\rho$) between the experimental (EXP) and single point (SP) models, mainly around intermolecular bonded carbonyls. Further investigation via molecular electrostatic potential maps reaffirmed the charge redistribution enhanced intramolecular hydrogen bonding, predominantly for N(2′) and N(2) (61.2 kJ mol-1 & 61.8 kJ mol-1 respectively). An overall weaker lattice energy of the triclinic form (-101.6 kJ mol-1) compared to the monoclinic form (-132.9 kJ mol-1) results in a lower threshold to overcome to initiate dissociation. Future work via physical testing of the novel co-crystal in both dissolution and solubility will further solidify the correlation between theoretical and experimental results.

Introduction

A co-crystal is defined as the combination of two chemical moieties in the same homogenous phase rather than two individual crystalline phases mixed together.[1] In the pharmaceutical industry, a co-crystal is usually the combination of an Active Pharmaceutical Ingredient (API) and a second molecule known as a coformer, which is added to enhance the API's properties such as stability and solubility. The coformers in co-crystals are often

inactive ingredients but there are numerous co-crystals emerging where the API is combined with another API, such as tramadol hydrochloride in combination with celecoxib for pain management[2].

Co-crystallisation of APIs has been of increased interest due to its advantages over simple salt formations when attempting to increase solubility; where poor solubility is one of the main reasons that interest in potential drug candidates is discontinued.[3-13] Salt formation is one of the most common methods of modifying physical properties of an API,[14] and an obvious requirement is the existence of an ionisable functional group within the API.[8] Co-crystals are an attractive alternative as the non-ionisable molecules can be combined with a range of possible coformers, such as carbamazepine and saccharin which exhibited a similar bioavailability to commercial carbamazepine with a lack of polymorphism, therefore enhancing stability.[15] Furthermore, without the need to facilitate the ionic center of an API we can utilise a larger number of coformers which in turn vastly increases the number of potential APIs suitable for potential co-crystal formation.

Numerous co-crystals have been studied to identify the extent to which solubility and other properties are altered upon co-crystallisation,[4, 10, 12, 16, 17] again, the carbamazepine and saccharin co-crystal which exhibited an increased solubility over the non-ionic carbamazepine alone.[18] Co-crystallisation can also be applied to ionisable APIs to enhance physicochemical properties such as exhibited in Haeria *et al.* [19], where an addition of a nicotinamide coformer to aspirin increased its solubility in the aqueous phase. This increase in solubility enhances the potential for permeable aspirin in solution to be absorbed by patients. Furthermore, partial correlations between aqueous solubility and melting points[20] have encouraged an even greater investigation into the relationship between melting point and chemical structure [21, 22]. A more developed understanding of the correlation between these two properties will enhance the clinical application of papers such as Wenger *et al.* [23],

who identified an increase in melting point for a co-crystal of gabapentin with oxalic acid, compared to gabapentin alone.

These promising results highlight the enhancement of APIs physical properties *via* co-crystallisation and lead to real-world applications, such as a more efficient absorption of medication by the body due to increased solubility meaning less API is needed for the same equivalent therapeutic action, or an increased shelf-life. Pharmaceutical options for co-crystallisation are vast, with the prerequisites for combining them to a coformer including complementary moieties and the formation of additional intermolecular interactions, such as van der Waals forces, aromatic donor-acceptor interactions and hydrogen bonding.[24]

Optimal targets for co-crystallisation are APIs that currently are discarded due to their unfavourable properties, such as a limited bioavailability, a narrow therapeutic range, or even a high side effect profile. Charge density studies of co-crystals and their polymorphs provide further information on the coformer-API interaction; chemical patterns derived from such studies, and their influence on respective physical properties, allow the development of optimised predictive methods for future coformer selection and/or design. Application of co-crystallisation, coupled with charge density studies will allow the opportunity to overcome physical barriers such as solubility and stability, without the need for expensive physical formulation trials.

Theophylline (Figure 1a) is a prime example of an API that has a range of disease applications despite its limitations. It is used as a bronchodilator in the management of reversible airway obstruction, such as in asthma[25], however issues such as its narrow therapeutic range[26] requires close monitoring[27]. Furthermore, high hygroscopicity reduces its stability[28], limiting the pharmaceutical shelf life, and protection from hydration damage.

Theophylline is thus regarded as a last line therapy for patients who are not managed effectively by other bronchodilators.

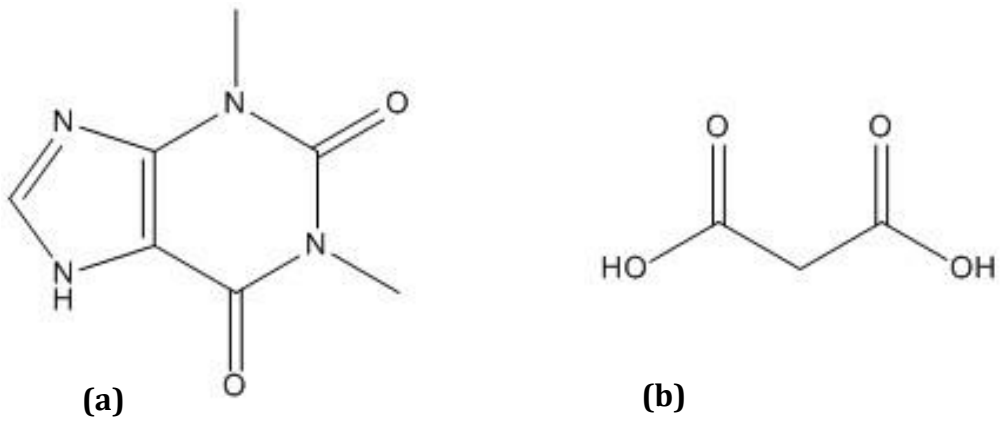

Figure 1 – Theophylline (**a**) and Malonic Acid (**b**) chemical structure

Although theophylline has a high hygroscopicity, it still has low solubility in water[29]. Hygroscopicity refers to the tendency of water to be reversibly adsorbed onto the surface but not directly integrated amongst the crystal lattice structure [30]. Thereby, solubility can be impacted due the crowding of the theophylline surface due to water adsorption at high relative humidity. Numerous papers have identified the possible co-crystal options such as theophylline-benzamide[31] and theophylline-acetylsalicylic acid[32]. Further papers have also illustrated the benefits of co-crystallisation for theophylline such as phase stability at 95% RH and solubility enhancement[33, 34]. Evarsti *et al.* illustrated the positive influences co-crystallisation *via* nicotinamide with anhydrous theophylline, even in humid conditions as, when left alone, the anhydrous theophylline readily transformed to the monohydrate form[35], whereas the co-crystal was more stable to hygroscopic effects.

Co-crystals provide a potential route towards API optimisation, but require a further analysis of weak interactions within the system[36]. Common themes across recent co-crystal studies have investigated the physical property enhancement of co-crystallisation but the

chemical explanation for the property alteration has largely not been identified. Charge density studies may provide the necessary tools to highlight weak interaction patterns across organic structures;[36-48] future coformer selection requires a strong understanding of how the physical properties are influenced by these interactions.[17, 49, 50]

In this study, high resolution X-ray crystallography was used to obtain the experimental electron density distribution (EDD) of a new polymorph of a 1:1 theophylline-malonic acid co-crystal. The use of malonic acid stems from previous studies identifying successful co-operation between molecules; its toxicity profile would not support its application as a coformer for human consumption in association with theophylline, so it is used here as an exemplar. The use of charge density studies is pivotal in streamlining the co-crystallisation techniques of the future, providing a more economical alternative to the currently expensive and inefficient hit and hope methods.

Methods

Theophylline and malonic acid were purchased from Merck (Castle Hill, NSW) and used without further purification. The method of crystallisation was taken from Trask *et al*. [51] where the same co-crystal in the monoclinic form was first reported. Equimolar amounts of theophylline and malonic acid in chloroform: ethanol (20:1) were heated to aid dissolution. The solutions were then combined and allowed to evaporate at room temperature.

Data collection, integration and reduction

Single-crystal X-ray diffraction experiments were carried out in the School of Pharmacy at the University of Sydney using a Rigaku SuperNova™ X-ray diffractometer with an X-ray wavelength of 0.7107 Å (Mo*K*α) at 150K. A crystal with dimensions 0.3 x 0.2 x 0.15 mm was mounted on a thin glass fibre with Paratone-N oil used as both an adhesive and cryoprotectant. Data was collected using 1° ω-scans with the crystal-to-detector distance kept

at 5.3 cm. Reciprocal space coverage was obtained by positioning the detector arm at 41.6 & 90.5°. A total of 9102 frames were collected.

Integration and reduction of the collected data were performed with the CrysAlis^{Pro} software package.[52] All crystals were cooled to 150 K with an Oxford Cryosystems COBRA cooler. The unit cell parameters for (**1**) were refined from 38971 reflections in the triclinic space group $P\bar{1}$ with Z' = 4, $F(000)$ = 592 and μ = 0.132 mm^{-1}.

Data reduction and refinement strategies

Atomic positions and anisotropic displacement parameters from the IAM model were then imported into XD[53], a program that models the electron density in the form of the Hansen-Coppens multipole formalism[54] with a least squares procedure being used to reach convergence. The formalism describes the electron density as the sum of aspherical pseudo atoms which are accompanied by its own electron density with nuclear positions $\mathbf{r}_j$ as shown in Equation (1).

$$\rho(\boldsymbol{r}) = \sum_j \rho_j \left(\boldsymbol{r} - R_j\right) \quad \textbf{(1)}$$

The complete density of the pseudo-atomic model is modelled by Equation (2).

$$\rho_j\left(\boldsymbol{r}_j\right) = P_c\rho_c + \kappa'^3 P_v\rho_v(\kappa'\boldsymbol{r}) + \kappa''^3 \sum_{l=0}^{l_{max}} \sum_{m=-l}^{m=1} P_{lm}R_l\,(\kappa''\boldsymbol{r}_j)d_{lmp}(\theta_j,\phi_j) \quad \textbf{(2)}$$

The expression for the pseudo-atom density can be separated into three portions; a term to describe the spherical core, a term to describe the valence density or that involved in bonding and finally a deformation term which describes the asphericity of the valence density. Radial

functions $\{R_l(\boldsymbol{r}_j)\}$ are used to model the behaviour of the valence shell of each pseudoatom. These functions are defined by angular functions $\{d_{lmp}(\theta_j, \phi_j)\}$ which are in turn defined by axes centred on each atom. The axes can differ between atoms. A variety of radial functions can be used, with the most common being Slater-type functions given in Equation (3).

$$R_l(\boldsymbol{r}) = Nr^{nl}\exp(-\varsigma_l \boldsymbol{r}) \quad \textbf{(3)}$$

The structure of (**1**) was solved using direct methods using SHELXT.[55] A full-matrix least-squares refinement based on F^2 was performed using SHELXL.[55] Bond lengths between non-hydrogen atoms to hydrogen atoms (X-H bonds, where X=C, O, N) were fixed at average values obtained from neutron diffraction studies, taken from Allen *et al*.[56] O−H, N−H, and bond lengths were set at 0.967 and 1.009 respectively. Aromatic C-H, CH_2 and methyl C-H bonds were set at 1.083, 1.092 and 1.059 Å, respectively, with bond vectors taken from the original riding H-atom models in the IAM refinement. All non-hydrogen atoms were refined anisotropically.

The multipole refinement process was carried out using the XD2006 program[53]. It was initiated with a refinement of the higher order data (usually $\sin\theta/\lambda > 0.8$ A^{-1}), which provides accurate atomic coordinates and temperature factors. These factors are used as the basis of the refinement. Refinement of the multipoles was carried out in a stepwise manner with C, O and N atoms being truncated at the octupolar level (l_{max} = 3) and hydrogen atoms were modelled using a single monopole and a bond directed dipole (l_{max} = 1). All non-hydrogen atoms were assigned a spherical function which governs the expansion and contraction of the valence shell to achieve the most accurate modelling of the electron density (κ') and a κ'' value was also introduced which models the aspherical expansion and contraction. Reflection statistical weights were applied with a default value of a = -2 as set by XDINI. For the refinement of F^2, Equation (4) illustrates the weighting scheme as implemented in SHELXL is used[57]:

Weight a [−2.0] b [0.0] c [0.0] d [0.0] e [0.0] f [1/3]

$$\omega_2 = q/[{s_2}^2 + (ap)^2 + bp + d + e\ x\ \sin(\theta)] \qquad \textbf{(4)}$$

Where:

$$s_2 = \sigma({F_0}^2)$$

$$p = f\ x\ {F_0}^2 + (1 - f)\ x\ {F_c}^2$$

$$q = 1.0 \text{ if } c = 0$$

$$\text{Or } q = \exp[c\ x\ (\sin\theta/\lambda)^2] \text{ if } c > 0$$

$$\text{Or } q = 1.0 - \exp[c\ x\ (\sin\theta/\lambda)^2] \text{ if } c < 0$$

The Hirshfeld rigid bond test was used to determine if the refinement was able to successfully deconvolute thermal motion from the electron density *i.e.* if the anisotropic displacement parameters have any actual physical significance[58]. This test measures the differences in mean-squared displacement amplitudes (DMSDA) with ADPs deemed to be described as physically meaningful if they are below 1 x 10^{-3} Å^2. The average value obtained for (**1**) was 5.56 x 10^{-4}Å^2, indicating an excellent deconvolution of thermal motion from the multipole model.

The scale, temperature factor and multipole populations were all refined separately during the refinement until the final cycles where they were combined to obtain the full variance-covariance matrix which is required to generate meaningful standard uncertainties (su). In all cases, all reflections were included in the refinement. Atomic coordinates, bond lengths and angles, anisotropic displacement parameters, hydrogen coordinates, and Torsion angles are available in Tables S1-S5 in the ESI.

Numerous refinements were conducted on the data with minor differences between end results. The refinement selected for this paper included all reflections and anisotropic temperature factors for the hydrogen atoms with no thermal diffuse scattering (TDS) correction. The data from other refinements and method for TDS correction conducted can be found in the ESI.

Refer to Table 1 for selected crystallographic information from the independent atom model (IAM) and multipole (EXP) refinements.

Anisotropic temperature refinement of hydrogen atoms

Hoser *et al*.[59] previously introduced the notion to also carry out a multipole refinement using anisotropic temperature factors for the hydrogen atoms to obtain a more accurate multipole model of the electron density. Anisotropic temperature factors for the hydrogen atoms were calculated using the SHADE3 server developed by Madsen[60]. The multipole refinement process was the same as above, with the only exception being that the hydrogen temperature factors were not refined.

Computational Methods

Gas phase, single point (SP) calculations were performed with geometry taken from the high-order experimental coordinates. All theoretical calculations were performed with the Gaussian 09 suite[61] at the CAM-B3LYP/6-311++G** level of theory for all structures. All calculations used the three-parameter hybrid exchange function developed by Becke [62] and Lee *et al.*[63] together with the long-range correction proposed by Tawada *et al.*[64, 65] (CAM-B3LYP). Analysis of the topology of electron density from the experimental model was performed using the XDPROP portion of XD2006 [53] while analysis of the electron density for the theoretical densities was performed using the DENPROP[66] program.

Results and Discussion

Geometry

The asymmetric unit (**1**) contains two molecules of theophylline and malonic acid in a 1:1 ratio [Figure (2)]. The triclinic form is previously unreported to our knowledge.

Table 1 - Selected crystallographic information for co-crystal (**1**)

Formula	$(C_7 H_8 N_4 O_2)_2$-$(C_3H_4O_4)_2$
Molecular Mass	568.47
Crystal size (mm)	0.3 x 0.2 x 0.15
Temperature (K)	150
Crystal system	Triclinic
Space group	$P\bar{1}$
a (Å)	7.946 (1)
b (Å)	12.426 (1)
c (Å)	12.889 (1)
α (°)	92.985 (1)
β (°)	104.179 (1)
γ (°)	101.477 (1)
Volume (Å^3)	1202.56 (2)
Z′	4
Refinement Method	Full-matrix least-squares on F^2
No. of reflections collected	225011
No. unique	38971
R_{int}	0.0344

Completeness (%)	98.6
No. reflections used	38971
ρ_c (g cm^{-1})	1.570
F(000)	592
μ (mm^{-1})	0.132
sin θ/λ_{max}	1.25
θ range for data collection (°)	3.365-62.644
Index ranges	$-19 \leq h \leq 19$ $-31 \leq k \leq 31$ $-32 \leq l \leq 32$
IAM Refinement	
N_{obs}/N_{var}	85.276
$R(F)$, $R(F^2)$, all data	0.0447, 0.1122
Final *R*1, *wR*2	0.0356, 0.1072
Goodness of fit	1.022
Residual density (*e* Å^{-3})	-0.856, 1.183
Multipole Refinement	
N_{obs}/N_{var}	37.1861
$R(F)$, $R(F^2)$, all data	0.0379, 0.0309
$R(F)$, $R(F^2) > 3\sigma(F)$	0.0301, 0.0576
Goodness of fit	1.3971
Residual density (*e* Å^{-3})	-0.353, 0.246

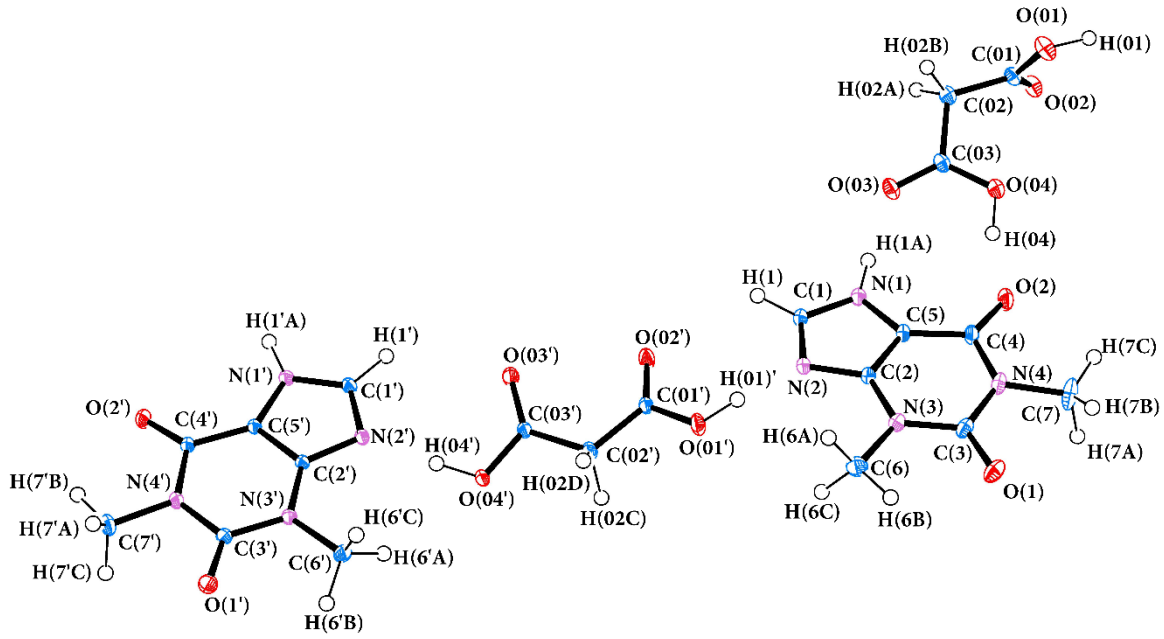

Figure 2 - ORTEP diagram of theophylline malonic acid co-crystal (**1**). Thermal ellipsoids are shown at the 50% probability level. [67]

Topological Analysis

Topological analysis was carried out by applying the Quantum Theory of Atoms In Molecules (QTAIM) [68] with completion of the analysis ensured by satisfaction of the Poincaré-Hopf and the Morse relationships[69] for the single point (SP) and experimental (EXP) models respectively.

Table 2 lists the key results from the topological analysis of carbonyl bonds only in (**1**) comparing the EXP values against the SP as they displayed the biggest variation between experiment and theory. The full list of EXP values can be found in Table (S6) of the ESI.

Table 2 - Topological analysis of the carbonyl bonds only in co-crystal (**1**).

Bond	**Model**	**ρ (e Å^{-3})**	**∇²ρ (e Å^{-5})**	**ε (Ellipticity)**	**Δ ρ (EXP-SP)**	**Δ ∇²ρ (EXP-SP)**
O(2)--C(4)	*EXP*	2.95 (2)	-38.48 (9)	0.18	0.33	17.80
	SP	2.62	-20.68	0.06		
O(03)--C(03)	*EXP*	2.95 (2)	-39.05 (1)	0.23	0.21	15.79
	SP	2.74	-23.26	0.06		
O(1')--C(3')	*EXP*	2.92 (1)	-37.02 (9)	0.17	0.17	15.04
	SP	2.75	-21.98	0.11		
O(02)--C(01)	*EXP*	2.97 (2)	-37.26 (1)	0.27	0.22	14.65
	SP	2.75	-22.61	0.09		

O(02')--C(01')	*EXP*	2.94 (2)	-36.91 (1)	0.17	0.17	13.54
	SP	2.77	-23.37	0.08		
O(1)--C(3)	*EXP*	2.80 (2)	-35.40 (1)	0.17	0.04	13.30
	SP	2.76	-22.10	0.11		
O(03')--C(03')	*EXP*	2.90 (1)	-37.11 (1)	0.23	0.09	12.81
	SP	2.81	-24.30	0.08		
O(2')--C(4')	*EXP*	2.73 (1)	-31.73 (9)	0.11	0.01	9.64
	SP	2.72	-22.09	0.08		

A visual analysis of the outliers in Table 2, show they are the carbonyl bonds involved in intermolecular bonding as highlighted in Figure 3. Crystal packing effects may further influence the observed differences in $-\nabla^2\rho$ due to the SP model representing the isolated gas-phase molecules. Experimental error can also impact results with higher quality conditions upon data collection such as a lower temperature, exhibiting smaller differences between the EXP and SP models. Such examples can be seen in studies by Luger *et al.* who investigated single molecule crystals of thymidine[70] and sucrose[71] both collected at temperatures of 20K. One study examined the experimental charge density of sucrose in comparison to the theoretical model. The greatest Laplacian differences between the two models was a more negative value of 5.8e $Å^{-5}$ identified at both ether groups O(5)-C(1) and O(2')-C(2'). Whereas the thymidine study compared two separate invariom theoretical refinements (ITM and *meso*-ITM) of a thymidine crystal with a 'classical' multipole refinement (CRM). The results indicated an average Laplacian difference overall of 3.8 and 3.7e $Å^{-5}$ respectively between ITM and *meso*-ITM with CRM. However, the carbonyl double bonds between O1=C1 and O2=C2 portrayed significantly more negative Laplacian (~10e $Å^{-5}$) in the CRM when compared to both ITM and *meso*-ITM.

Similar differences for co-crystal **(1)** [collected at 150K] can be seen in Graphs S1-16 found in the ESI where the carbonyl groups electron density and the Laplacian in the EXP and SP models are compared. Commonly, the EXP model represents a greater degree of change in the Laplacian amplified from much smaller differences in electron density. The shallower gradient exhibited in Graphs S8 & S12 for the EXP results are probably due to the intermolecular bonding present within the EXP co-crystal reducing the strong polarity represented in the gas-phase SP model. The EXP model differing so considerably from the SP model can also be attributed to the repositioning of the bond critical point (bcp). Small differences in the location among these densities can be exaggerated considerably by the rapidly changing nature of the Laplacian [Graphs S3-S8]. Similar variations have been noted in previous charge density studies comparing the EXP and SP models of co-crystals and hydrates[72-74]. Notably, these results are commonly localised around covalent bonds that undergo hydrogen bonding when crystallised such as cytosine monohydrate in the study by Guru Row and Munshi[74]. A difference of around ~20e $Å^{-5}$ in the Laplacian value was recorded when experimental data (-39.77e $Å^{-5}$) collected at 90K was compared to the theoretical model (-19.67e $Å^{-5}$). This was located at the only carbonyl that underwent hydrogen bonding with a different molecule, water in this instance. These results are in line with the carbonyl groups present in co-crystal (**1**). In contrast, the 2-thiouracil from the same study presented minimal difference between the experimental data (-27.51e $Å^{-5}$) and the theoretical model (-28.72e $Å^{-5}$) when bound to another 2-thiouracil molecule on its only carbonyl group (1.21e $Å^{-5}$).

As illustrated in Figure 3, these carbonyls are all present on the malonic acid molecule and interact directly *via* hydrogen bonding with a theophylline molecule. The fourth and final carbonyl group [C(01)-O(01)] from the malonic acid constituent does not present a closed shell reaction. This is the only carbonyl to bond with another malonic acid and not a theophylline molecule.

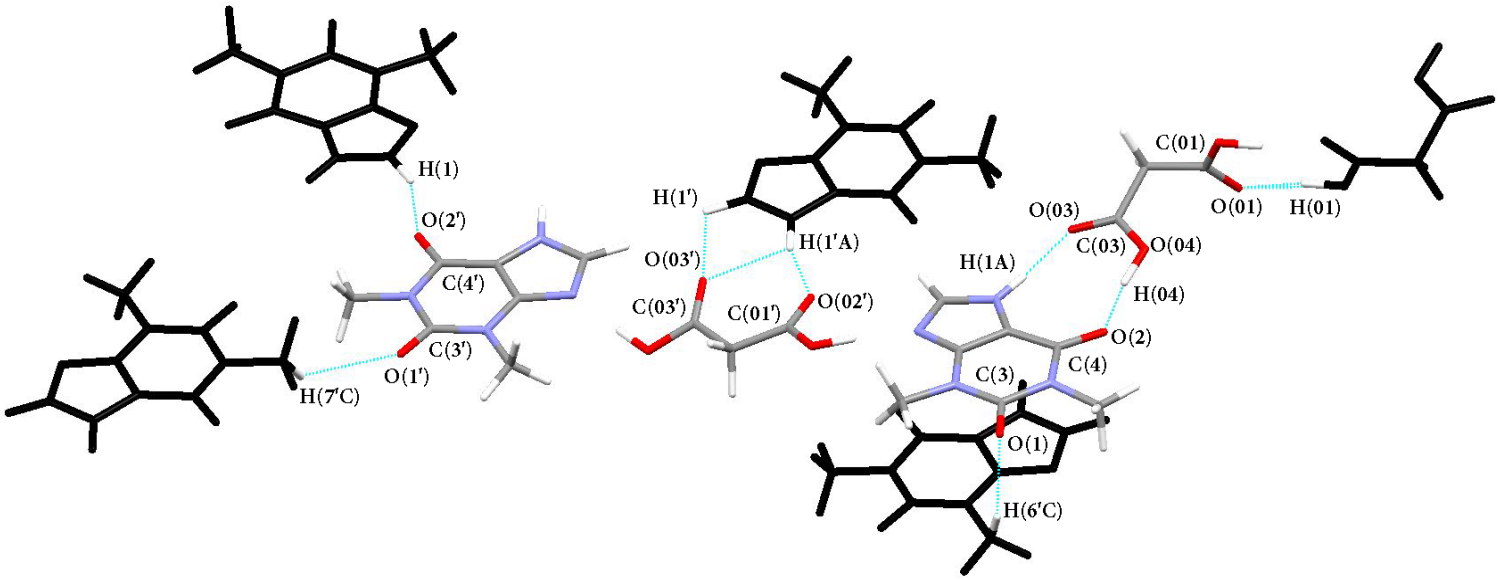

Figure 3 - Hydrogen bonds involving carbonyl groups within the co-crystal (**1**) illustrated using MERCURY [75-76]

The highest difference (17.80) between SP and EXP models reported in Table 2 was found at the O(2)–C(4) bond located on a theophylline molecule (SP -20.68 e $Å^{-5}$ & EXP -38.48 e $Å^{-5}$). Whereas, the second highest difference (15.79) neighbours this bond at O(03)-C(03), residing on the malonic acid bound to the theophylline molecule (SP -23.26 e $Å^{-5}$ & EXP -39.05 e $Å^{-5}$). Application of Cortes-Guzman *et al*'s [77] work on the valence shell charge concentration and its proportionality with $\nabla^2\rho$ indicates that the more negative value of the EXP model suggests a higher local electron density. This is supported in the contour maps of Figures 4 (a) and (b) comparing the Laplacian of the EXP and SP models of the bonding molecules.

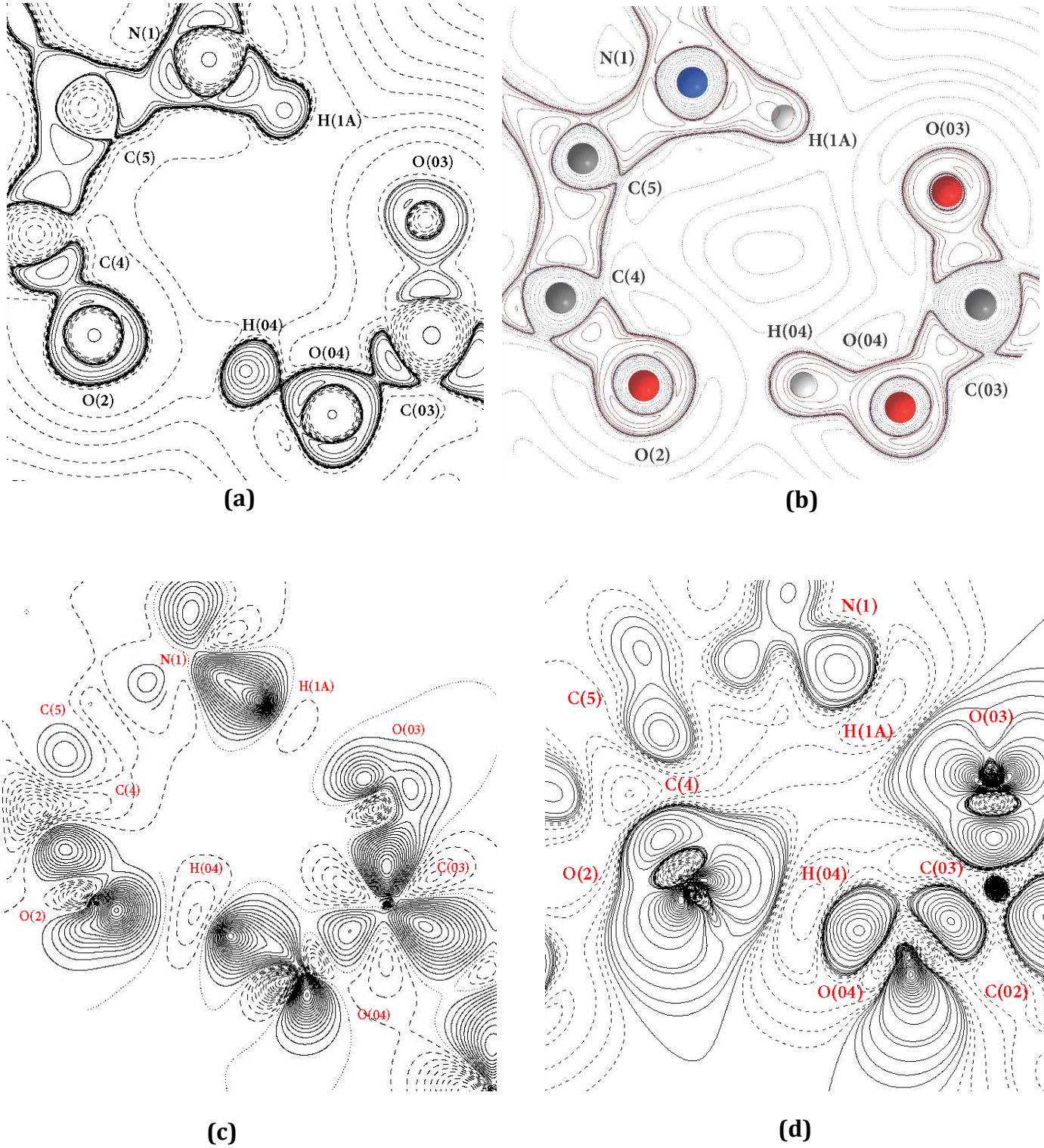

Figure 4 - $\nabla^2\rho$ diagram of the C(4)-O(2) and O(03)-C(03) bonds in (**a**) EXP and (**b**) SP models in co-crystal (**1**). Plane is defined by atoms C(03), O(2) and H(1A). Contours are plotted on a log scale (with range -800 to -0.001 and 0.001 to 800). Positive lines indicate positive contours and dashed lines indicate negative contours. The C(4)-O(2) and O(03)-C(03) bonds deformation density diagram in **(c)** EXP and **(d)** SP. Contours are plotted on a 0.01 scale (with range -3.5 to -0.1 and 0.1 to 3.5).

The clear pinching of the valence shell charge concentration (VSCC) at the C(4)-O(2) and O(03)-C(03) bonds shown in Figure 4(a) coupled with the negative $\nabla^2\rho$ value indicates a topology that is typically seen in bonds between carbon and electronegative atoms. The influence of this effect on the hydrogen bonding sites of O(2) and O(03) are discussed later.

The malonic acid molecule sandwiched between theophylline molecules within co-crystal **(1)** contains another notable difference of $\nabla^2\rho$ values in the bond O(02)-C(01) between the EXP and SP models. Again, we notice from the contours maps in Figure 5(a) and (b), a clear pinching of the VSCC in the EXP model as compared to the SP model. The polarisation of lone pairs on O(02) is shown with the contour pinching distinct in the EXP model Figure 5(a) as compared to the SP model in Figure 5(b). The important difference here is the influence of the neighbouring malonic acid unit in the co-crystal structure that facilitates the complementary geometry of the EXP model.

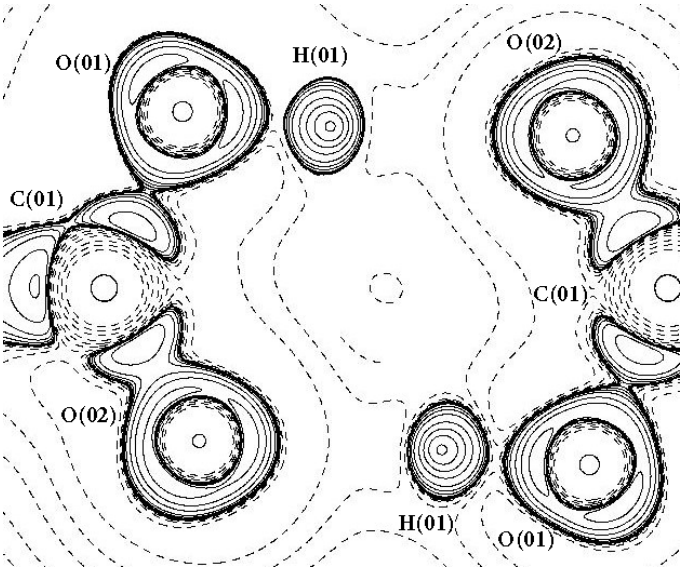

(a)

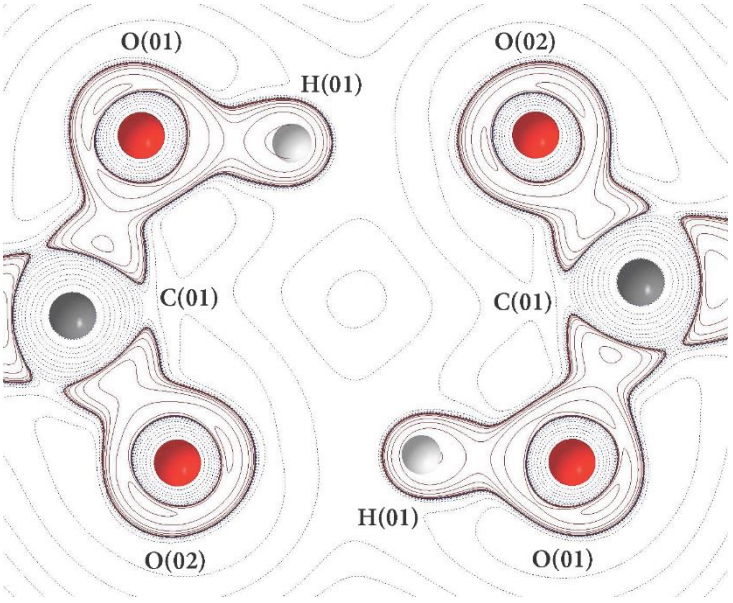

(b)

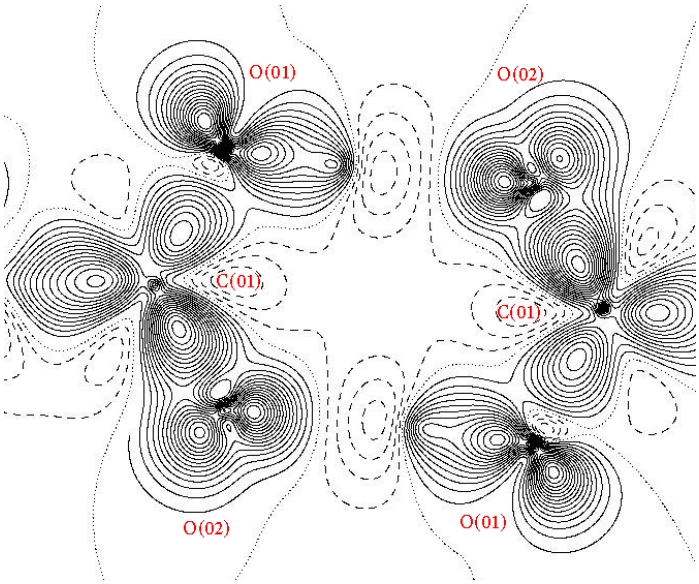

(c)

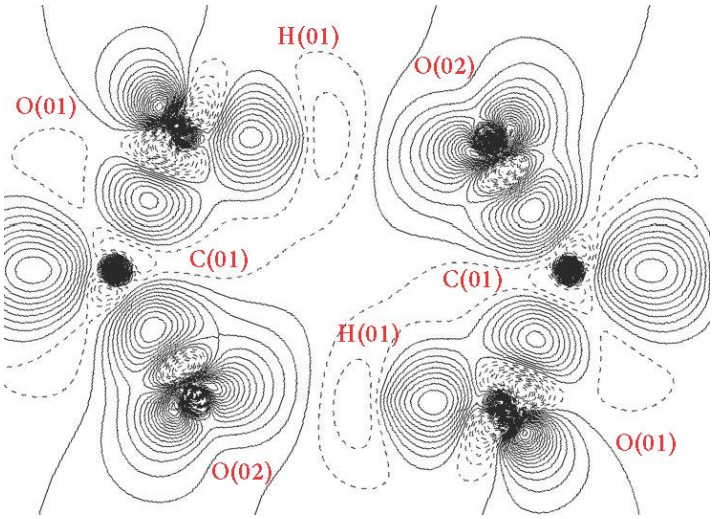

(d)

Figure 5 - $\nabla^2\rho$ diagram of the O(02)-C(01) bond in the EXP **(a)** and SP **(b)** models. Plane is defined by atoms C(01), O(02) and O(01). Contours are plotted on a log scale (with range -800 to -0.001 and 0.001 to 800). Positive lines indicate positive contours and dashed lines indicate negative contours. The O(02)-C(01) bond deformation density diagram in **(c)** EXP and **(d)** SP. Contours are plotted on a 0.05 scale (with range -3.5 to -0.1 and 0.1 to 3.5).

This orientation of the malonic acid molecules coincides with Goedkoop and MacGillavry's results, which showed the most favourable position was to have the ends mirrored to each other.[78] This orientation induces complementary stacking of the theophylline molecules [Figure 6(a)] within the co-crystal giving rise to aromatic donor-acceptor interactions, increasing the overall potential stabilisation energy. The same malonic bridge interaction is not present in the monoclinic theophylline malonic acid co-crystal [51].

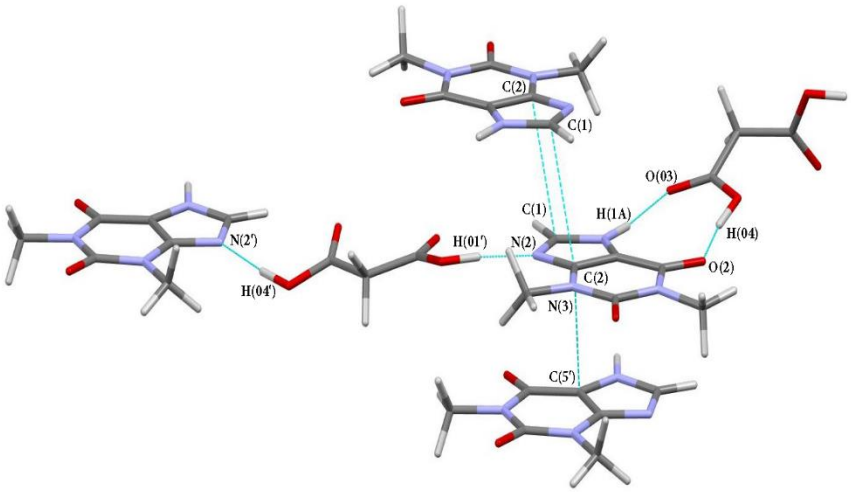

(a)

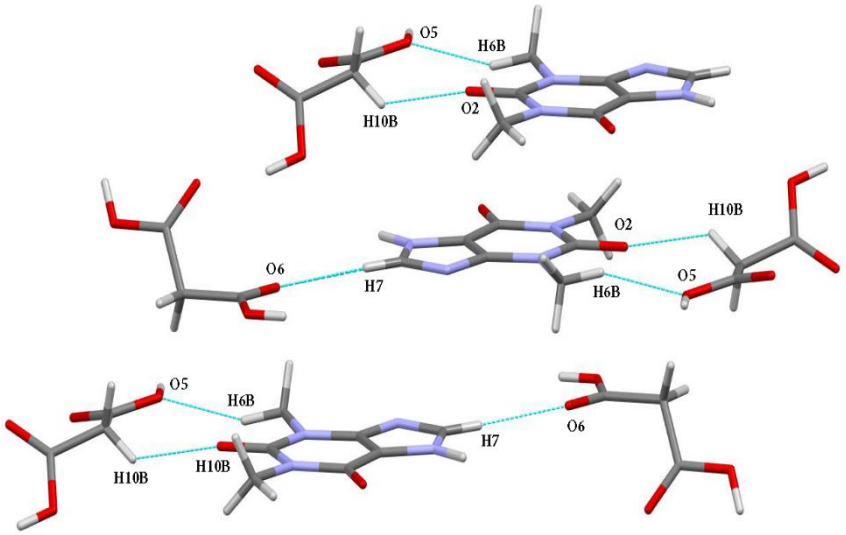

(b)

Figure 6 - Hydrogen bonding and aromatic stacking exhibited in (**a**) co-crystal (**1**); and (**b**) monoclinic theophylline and malonic acid [51] using MERCURY [76]

Hydrogen Bonds

Hydrogen bonding is another contributor to the overall potential stabilisation energy of co-crystal (**1**) with a number present throughout. The typical hydrogen bond is characterised by the interaction of a proton-donating bond and a proton acceptor involving electronegative atoms such as O, N and F.[79] The criterion for the presence of hydrogen bonds is generally the distance between the hydrogen atom and proton acceptor being less than the sum of their corresponding van der Waals radii.[80] This notion is exhibited in Figure 7, where the red spots on the Hirshfeld surface illustrate the instances the combined distance is smaller than the corresponding radii.

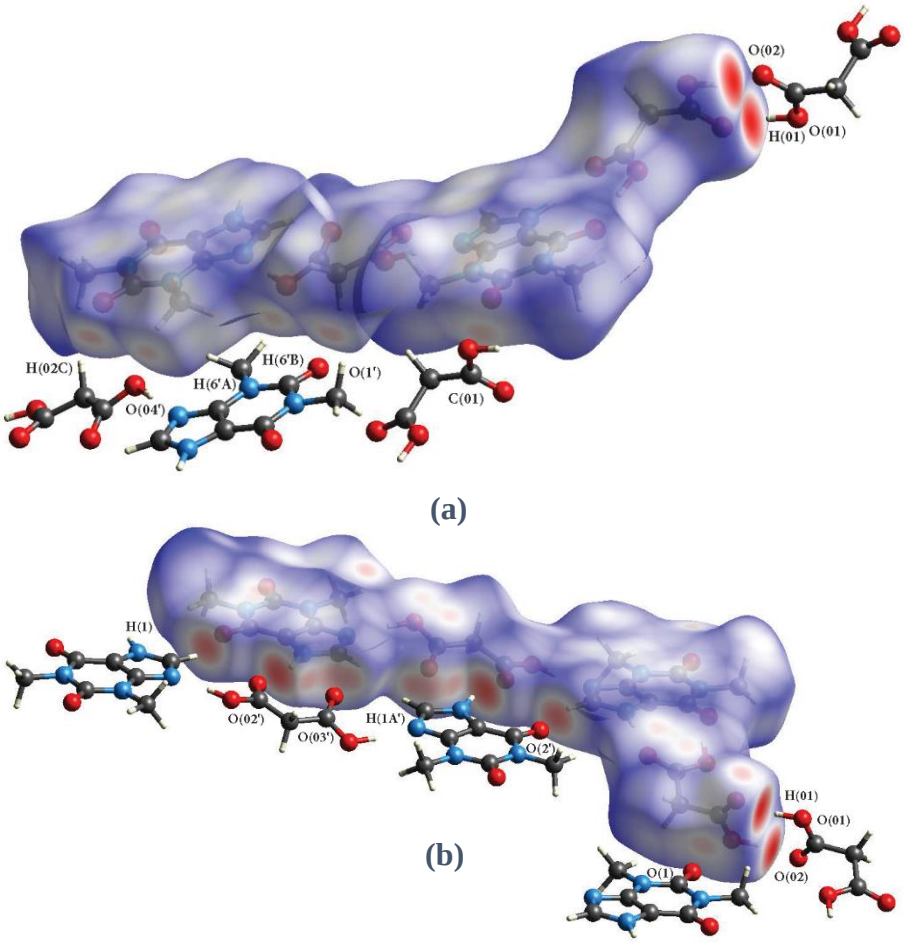

Figure 7 - Hirshfeld surface of co-crystal (**1**) from two different angles, (a) & (b) created and illustrated by CrystalExplorer [81]

Hirshfeld surface diagrams are visual depictions of the d_{norm} surfaces which are the sum of normalised van der Waals radii (d_e & d_i) of atoms involved in an interaction.[82] These van der Waals radii measure the distance from the nucleus to the surface of an atom (d_i) and from that surface to the nucleus of a neighbouring atom (d_e). The colours of the surface relate to the proximity of the atoms involved. As noted earlier; red identifies contacts closer than the sum of their van der Waals radii, whereas blue surfaces depict distances longer than the sum of their van der Waals radii and white show contacts equal to the sum of the van der Waals radii.[83] Coupling the contact distances shown in the Hirshfeld surface [Figure 7] with the molecules involved, we can identify the bond types between molecules and the percentage of surface attributed to each. Furthermore, the quantifying of interactions throughout a crystal lattice *via* the Hirshfeld surface analysis, identifies any surface contribution differences that can translate to altered physiochemical and/or physical properties.[84] This is especially vital when structural differences are very subtle but translate to costly errors, such as two polymorphic crystals with varying physiological effects.[85, 86]

Several hydrogen bonds are involved in the co-crystal formation, the full list is available in the ESI (Table S7 & S8). The ability of malonic acid to act as both hydrogen bond donor and acceptor allows it to bridge theophylline molecules as seen in Figure 3 and Figure 8. Aromatic stacking is also exhibited between theophylline molecules as shown in Figure 6 (a) and reinforced when analysing fingerprint plots of the structure [Figures 9 & 10].

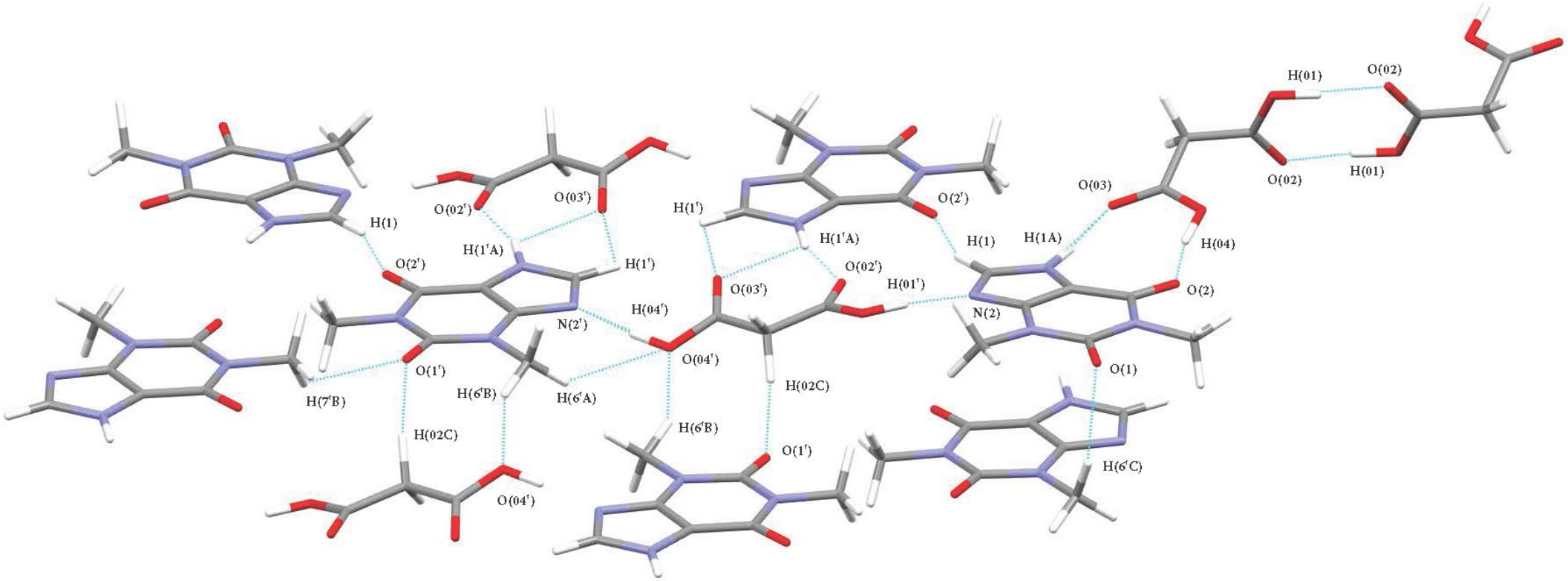

Figure 8 - Hydrogen bonding between malonic acids and theophylline molecules in co-crystal (**1**)

Hirshfeld surface diagrams illustrate the combined van der Waal radii distance, but fingerprint plots also identify the distance between the nucleus of each neighbouring molecule from the surface they share.[87] It does this by defining $d_{i,}$ the distance from the nucleus of an atom to its surface and d_e, the distance from its surface to a neighbouring atoms nucleus. Combination of these two values help map the intermolecular contact distances within the co-crystal. Fingerprint plots also calculate the percentage of surface involved in user specified atom-atom bonding. Fingerprint plots of the primary bonds involved in the geometric configuration of the triclinic co-crystal (**1**) have been included. A full display of all fingerprint plots from co-crystal (**1**) and the monoclinic form are listed in Figures S6 & S7 respectively in the ESI.

The fingerprint plots below in Figures 9 (a-b) illustrate distances of 3.2Å to 4.4Å which coincides well with literature regarding the average aromatic donor-acceptor interaction separation[88-89] . The total percentage of the co-crystal (**1**) surface involved in these aromatic interactions is 8.2%. Whereas Figures 10 (a-c) depict the more standard hydrogen bonding around the C, N and O atoms. The peaks highlighted in Figure 10(b) correspond with a d_{norm} distance of 1.7Å, indicative of the strong hydrogen bond found at O(2). The full distribution of surface area contributing to intermolecular bonding within the crystal structure is charted in Figure 11 (a). Another notable influence on the crystal packing is 31% of the Hirshfeld surface contributed *via* H···H bonds. This influence has been addressed previously in a study by Matta *et al*, which found that when neighbouring hydrogen atoms are at a distance less than the sum of their van der Waals radii, the proton attraction to the electron density distribution overcame the repulsive contributions resulting in a net positive change in stabilisation energy[90]. Further comparing of the numbers that formulate the fingerprint plots of the novel triclinic polymorph with the monoclinic form are displayed in Tables 3 & 4 and Figure 11 (a) and (b). The greater distribution of elements involved in the total surface

bonding by the triclinic form clearly reinforces the geometry complementarity. These numbers reflect a greater number of bonding motifs in the triclinic possesses over the monoclinic form, which can induce stronger hydrogen bonds.

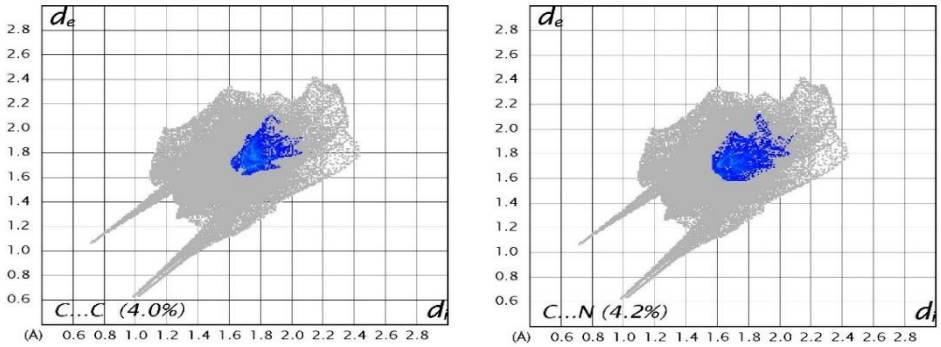

(a) **(b)**

Figure 9 - Fingerprint plot diagram of C···C interactions **(a)** and C···N interactions **(b)** in **(1)**

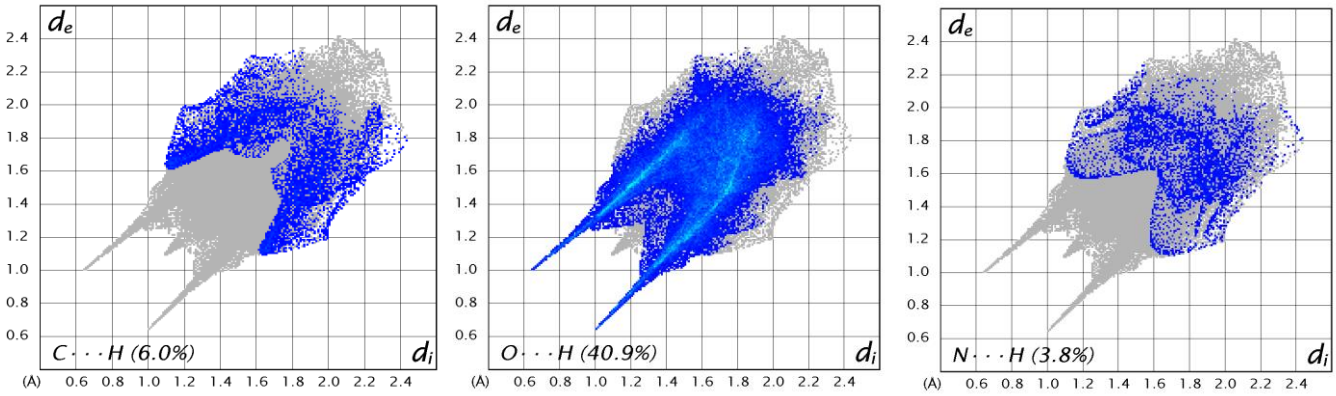

(a) **(b)** **(c)**

Figure 10 - Fingerprint plot diagrams of C···H **(a)**, O···H **(b)**, and N···H **(c)** interactions in **(1)**

Table 3 – Hirshfeld surface area included in bonding interactions for the triclinic co-crystal (**1**)

Triclinic Form	**C**	**N**	**O**	**H**
C	4%	4.2%	6.5%	6%
N		1.7%	1.6%	3.8%
O			3.1%	40.9%
H				31.4%

Table 4 – Hirshfeld surface area included in bonding interactions for the monoclinic theophylline and malonic acid co-crystal

Monoclinic Form	**C**	**N**	**O**	**H**
C	1.1%	2%	3.8%	5.3%
N		0.7%	0.7%	2%
O			1.3%	42.4%
H				32.8%

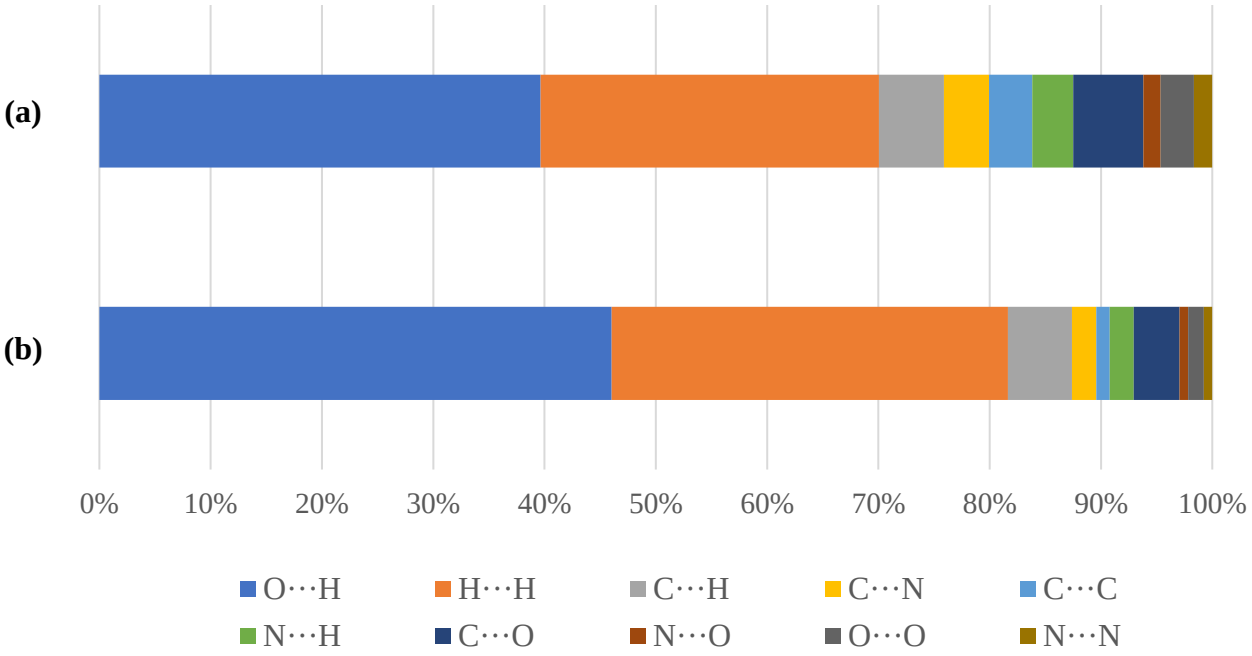

Figure 11 – Distribution of the Hirshfeld surface percentage involved in bonding both inside and outside the unit cell. (**a**) Triclinic theophylline and malonic acid co-crystal (**1**) & (**b**) Monoclinic theophylline and malonic acid co-crystal

Grabowski's study of hydrogen bond strength,[91] identified through factor analysis, indicated a better correlation between the parameters of the donor to hydrogen distance (D-H) and hydrogen bond strength rather than those of the acceptor. These parameters included the bond length, electron density at the bcp of D-H and the Laplacian at that density. The E_{HB} and D-H factors accounted for more than 95% of the total variance in samples examined. We therefore can theoretically predict the influence a hydrogen bond will have on a co-crystal without knowing the actual environment of the reference molecule. The caveat however, is that such knowledge is more applicable to studies utilising X-ray-neutron results combined with X-ray diffraction (X-N Studies) than X-ray diffraction alone due to the D-H distance accuracy being higher with the former. The applications of the hydrogen bond results present in the EXP model as listed in Table 5, provide a more comprehensive understanding associated with hydrogen bonding in co-crystal formation when compared with theoretical data.

Abramov and Espinosa's method suggests the local kinetic and potential energies (*G* and *V*) and the total density (*H*) at bond critical points in hydrogen bonds can be determined from the density property *V*, and therefore can be used as a measure of bond strength.[92, 93] This method was used to estimate the strengths of these hydrogen bonds (E_{HB}).

Table 5 - Topological analysis of hydrogen bonding in (**1**)

Bond	ρ (e Å^{-3})	$\nabla^2\rho$ (e Å^{-5})	$d_{H\cdots bcp}$ (Å)	$d_{A\cdots bcp}$ (Å)	G (Ha/Bohr^3)	V (Ha/Bohr^3)	H (Ha/Bohr^3)	E_{HB} (kj mol^{-1})
C(1)-H(1)···O(2')[a]	0.09 (11)	2.11 (4)	0.7805	1.2856	0.11	-0.08	0.03	15.3
C(1')-H(1')···O(03')[a]	0.11 (2)	1.53 (1)	0.9945	1.297	0.09	-0.08	0.01	15.0
N(1')-H(1'A)···O(02')[a]	0.16 (16)	3.37 (11)	0.6767	1.1816	0.20	-0.16	0.04	30.5
N(1')-H(1'A)···O(03')[a]	0.09 (1)	1.27 (1)	1.347	1.0422	0.07	-0.06	0.01	11.7
C(6')-H(6'A)···O(02)[b]	0.05 (3)	0.84 (1)	1.4317	1.0486	0.05	-0.03	0.01	6.2
C(6')-H(6'B)···O(04')[c]	0.03 (3)	0.59 (1)	1.5324	1.0939	0.03	-0.02	0.01	3.5
C(6')-H(6'C)···O(1)[d]	0.05 (4)	0.67 (1)	1.4638	1.0586	0.04	-0.03	0.01	5.0
C(6')-H(6'C)···O(02)[e]	0.05 (2)	0.67 (1)	1.4452	1.1154	0.04	-0.03	0.01	5.3
C(7')-H(7'C)···O(1')[f]	0.06 (1)	0.85 (1)	1.4256	1.1707	0.05	-0.04	0.01	7.0
C(02')-H(02D)···O(04)[g]	0.04 (2)	0.54 (1)	1.5345	1.1594	0.03	-0.02	0.01	3.6

O(01)-H(01)···O(02)[h]	0.21 (21)	5.38 (30)	1.1258	0.5184	0.31	-0.24	0.07	47.6
N(1)-H(1A)···O(03)	0.18 (19)	4.06 (16)	0.637	1.1687	0.24	-0.19	0.05	36.9
C(6')-H(6'A)···O(04')	0.05 (2)	0.66 (1)	1.1288	1.6533	0.04	-0.03	0.01	5.2
O(04)-H(04)···O(2)	0.30 (24)	6.86 (33)	0.5333	1.0726	0.43	-0.38	0.05	73.9
O(01')-H(01')···N(2)	0.24 (24)	7.36 (38)	0.4984	1.1449	0.42	-0.32	0.10	61.8
O(04')-H(04')···N(2')	0.25 (23)	6.47 (36)	0.5056	1.1441	0.38	-0.31	0.07	61.2
C(02')-H(02C)···O(1')[i]	0.05 (4)	0.90 (1)	1.4178	1.0312	0.05	-0.03	0.01	6.4

[a] 1-x, *1*-y, *1*-z; *[b] 2*-x, *2*-y, *-1*-z; *[c] 1*-x, *-1*-y, *1*-z; *[d] 1*-x, *-1*-y, *-1*-z; *[e] 1*-x, *2*-y, *-1*-z; *[f] 1*-x, *-1*-y, *2*-z; *[g] 2*-x, *1*-y, *-1*-z; *[h] -2-x, -2-y, 1-z; [i] -1-x, -y, -1-z*

As seen in Table 5, the three strongest intermolecular hydrogen bonds: O(04)-H(04)···O(2), O(01')-H(01')···N(2) & O(04')-H(04')···N(2') (73.9 kJ mol^{-1}, 61.8 kJ mol^{-1} & 61.23 kJ mol^{-1} respectively) link each molecule within the asymmetric unit. These hydrogen bonds are also the shortest in length from the hydrogen atom to acceptor (H···A 1.598, 1.638 & 1.647Å respectively) which is in accordance with the notion of bond length influencing strength i.e. shorter hydrogen bonds are often stronger.[94] These results are further supported through analysis of enrichment ratios in atomic contacts.[95] The strongest were identified as H···O and H···N which is in accordance with the bonding seen in co-crystal (**1**). The strongest hydrogen bond between asymmetric units was found at O(01)-H(01)···O(02) on the malonic acid bridge as mentioned earlier.

The malonic acid bridge provided a very high stabilisation energy of almost 100 kJ mol^{-1} combined across both hydrogen bonds. This high strength leads us to believe these are the primary intermolecular bonds in orientating the asymmetric units together as seen in Figure 12(a). Complementary orientation noted by Goedkoop and MacGillavry is supported when we examine the almost linear (172°) bond angles between the unit cells across this malonic acid bridge. Furthermore, the higher enrichment of the carbonyl group in comparison to the hydroxyl group in carboxylic acids plays a more pivotal role in crystalline structure formation as identified in a study by Jelsch and Bisseyou.[45] The study analysed the tendencies for contact formation between hydrocarbon compounds when substituted with oxygenated chemical groups *via* an enrichment ratio. The high resulting ratio for oxygen atoms containing a double bond can be extrapolated to coformer selection over molecules containing weaker, single bonded oxygen atoms such as those in the carboxylic acids.

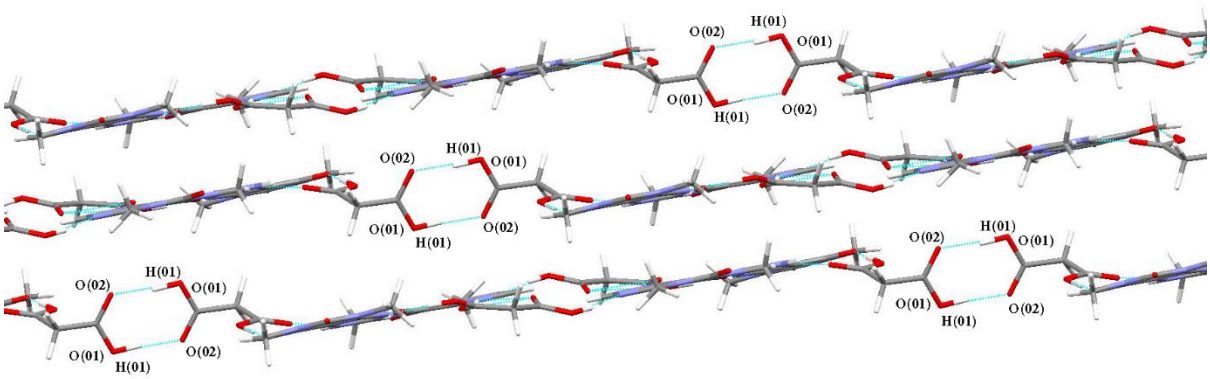

(a) Malonic acid bridges orientating the packing of the co-crystal (**1**)

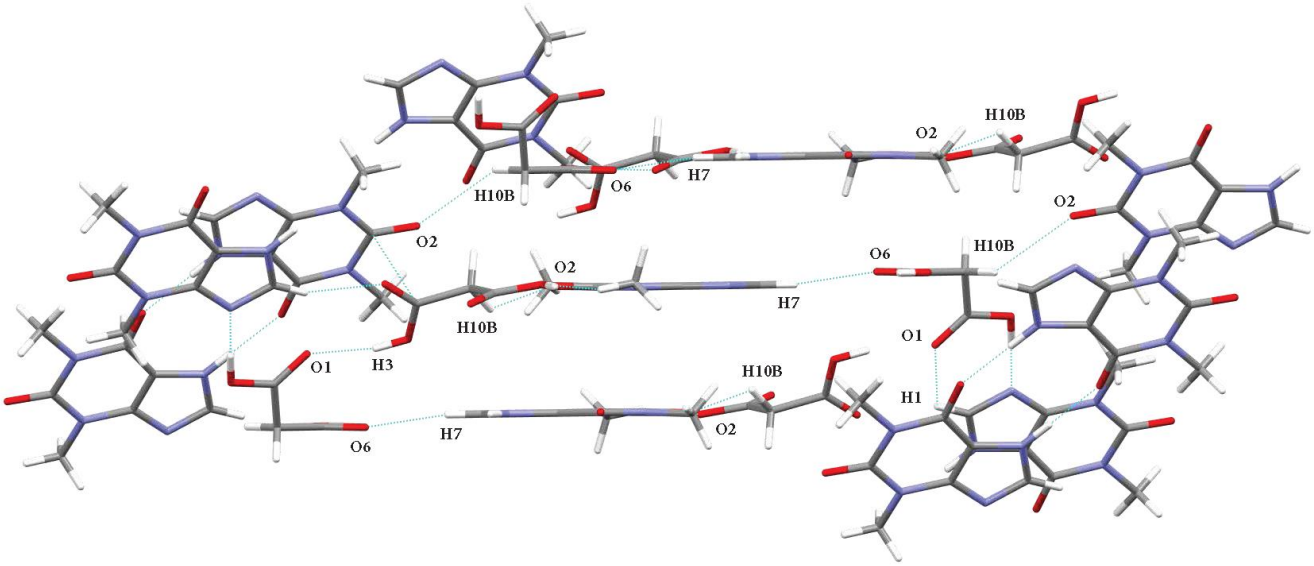

(b) Staggering of the malonic acid and theophylline is visible when extending past the unit cell for the monoclinic form

Figure 12 – Co-crystal structures of the (**a**) triclinic and (**b**) monoclinic theophylline and malonic acid co-crystal forms. Structures were illustrated using the MERCURY software[76].

As mentioned, intramolecular bonding influences the geometric coordination of the co-crystal. However, this also results in a direct influence on the availability of free space within the structure. This free space is termed the void space and is primarily the accessible regions within a molecule for solvents to attach or insert during any dissolution or solvation. The void space can be calculated *via* several methods. The most accurate method involves

rolling a probe sphere of a user defined set radius across the promolecule density surface[96]. The software program CrystalExplorer provides the ability to both generate the promolecule surface and run the void calculation. For co-crystal (**1**), the promolecule surface wavefunction was generated using the electron density at an isovalue of 0.002 a.u. as recommended by Turner *et al.* [97]. The Hartree-Fock method was used with a basis set 6-31G* for these calculations. The resulting percentage of promolecule density within the unit cell volume is 89.94%. The sum of the individual molecules within co-crystal (**1**) exceeded the difference between the total unit cell volume and the void space volume due to the overlapping of electron densities in the procrystal. As illustrated in Figure 13, the pockets of void space are localised away from the influential strong intramolecular hydrogen bond region. The colour scheme represents the proportion of isolated void space within a region of the unit cell. The most interesting regions are the red and orange, which represents surface areas of 189.97Å^2 and volumes of 53.38Å^3. Whereas the remaining colours all represent surface areas and volumes less than 11.38Å^2 and 3.42Å^3 respectively. This is further illustrated in Figure 14(a), *via* the Mercury program, using a rolling probe radius of 0.8Å on the solvent accessible surface. The smaller radius was used as the standard size (1.2Å) resulted in a 0% void volume due to the void spacing being too small for a single water molecule to penetrate. PLATON software was also used to examine the capability of other sized solvents to penetrate the spacing within the co-crystal (**1**) with a resulting 0% void volume[98]. The promolecule density analysis was run on the anhydrous form of theophylline that was retrieved from the CDCC [BAPLOT01][99]. The promolecule density volume result is 86.97%. This is to be expected with co-crystallisation proving successful in physicochemical enhancement in numerous papers such as the reduction in hygroscopicity of theophylline reported by Trask *et al.* when co-crystallised with dicarboxylic acids[51]. When comparing results of the novel triclinic theophylline malonic acid polymorph from this study with the monoclinic form found in

Trask *et al.*, we found an increase in promolecule density of ~1.64% (89.94% vs 88.30% respectively). A variety of isovalues were utilised to examine the void volumes of the triclinic and monoclinic co-crystals plus the single anhydrous theophylline form as listed below in Table 6. The validation of the 0.002 au void surface implemented in CrystalExplorer for void estimation is carried out in the study by Turner *et al.* [97]. The paper identifies a reliability between results gathered using He pycnometry and the CrystalExplorer software when examining porosity of crystalline material by Soldatov *et al.* [100]. The key features when examining the void volume percentages in Table 6 are the similarity between the monoclinic and anhydrous single theophylline form at all isovalues and the triclinic form at the 0.0003 au size, expressing the greatest void volume percentage of the three. As mentioned earlier, the intermolecular bonding between the malonic acid bridges within the triclinic form bundles the void which is evident predominantly at a smaller probe radius. As the radius size increases in Table 6 however, the greater number of bonding motifs on the surface of the triclinic form to restrict the void volume to 9.52%. In contrast, the monoclinic form does not possess the same surface bonding distribution and thus the void volume increases to a larger 10.49%. These results infer the overall stability increase in the triclinic form, would lead to a favourable reduction in hygroscopicity for storage and hence stabilisation from hydration. To further appreciate any physicochemical enhancements the new polymorph provides; physical testing such as dissolution and storage at varying relative humidity would be necessary in future experiments.

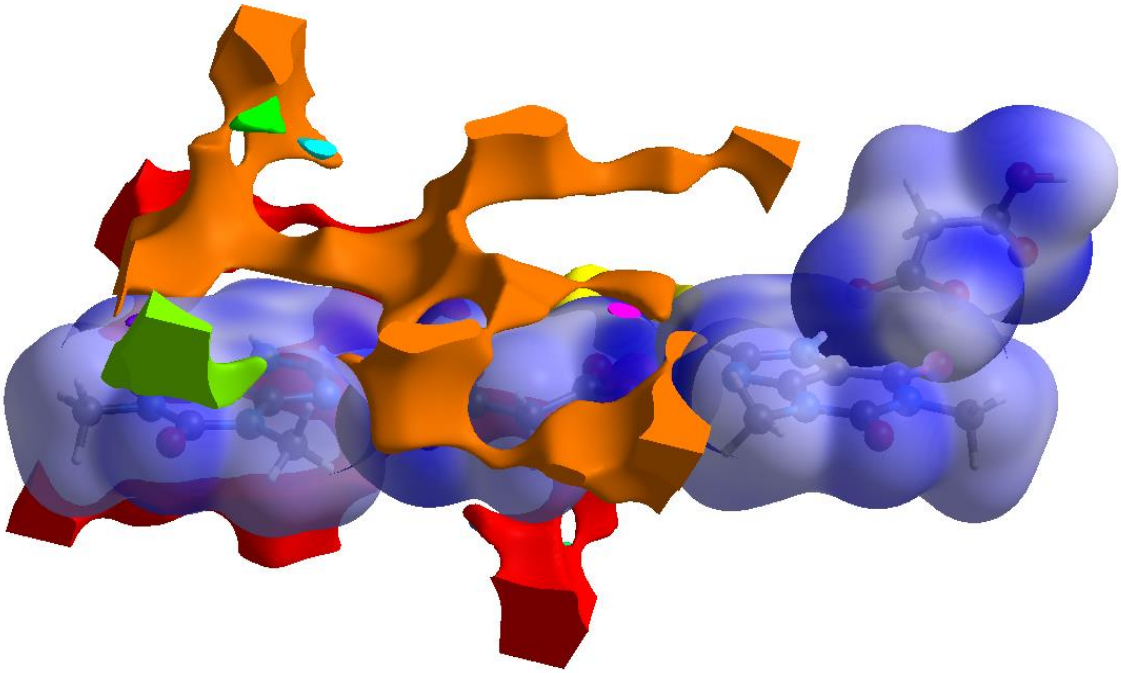

Figure 13 – Voids of co-crystal (**1**) at 0.002 a.u. isosurface. The volume occupied by the voids represents 9.52% of the unit cell volume[81].

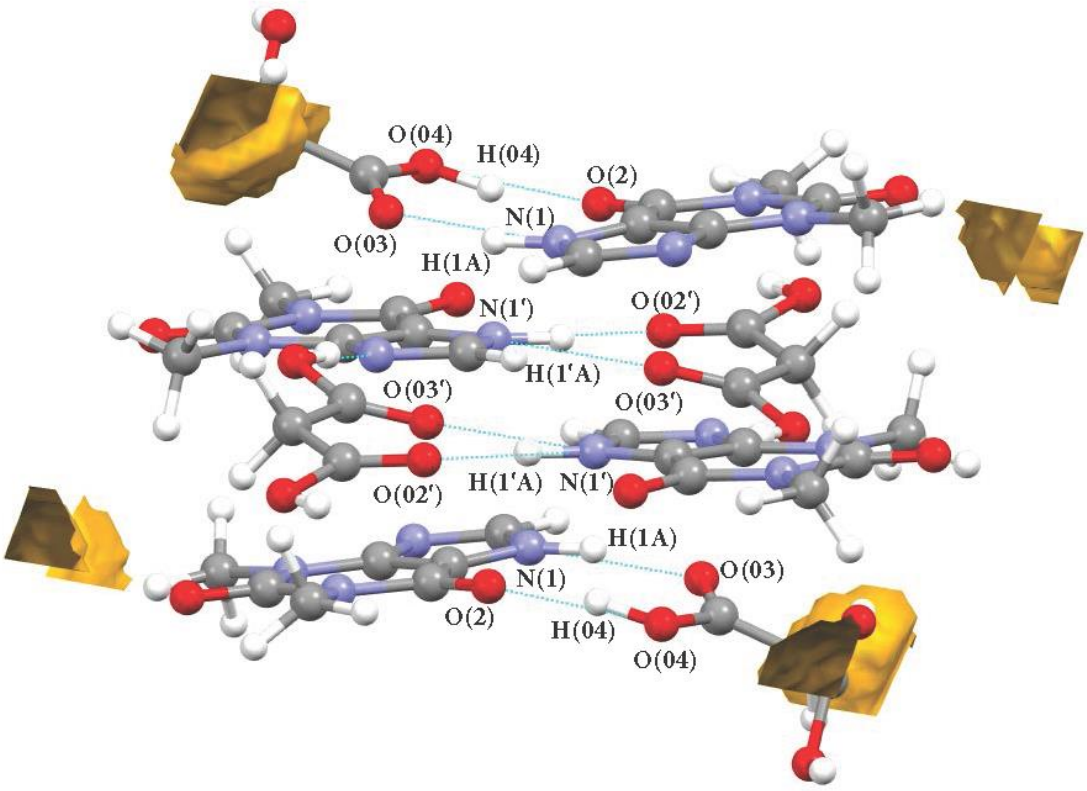

(a)

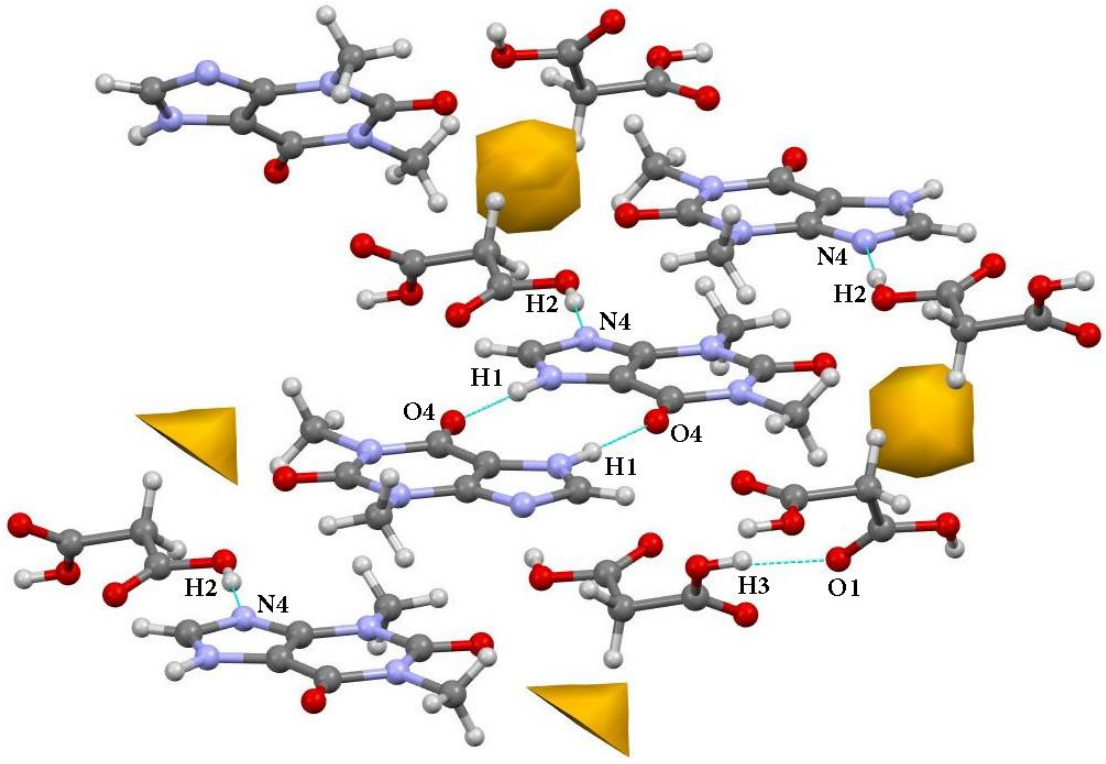

(b)

Figure 14 - Void space of (**a**) co-crystal (**1**) and (**b**) monoclinic theophylline and malonic acid within the Mercury program at a probe radius of 0.8Å[76].

Table 6 - Cell volume, surface area and percentage of total void volume for co-crystal (**1**), monoclinic theophylline malonic acid co-crystal and anhydrous theophylline calculated *via* different isovalue size probes. Results collected using CrystalExplorer software.

	Isovalue/au	**Volume/Å^3**	**Surface Area Å^2**	**% of Cell Volume**
Co-Crystal (1)	0.002	114.50	410.84	9.52%
	0.001	31.92	138.84	2.65%
	0.0005	6.79	29.55	0.56%
	0.0003	2.31	11.06	0.19%
Monoclinic Theophylline and Malonic Acid	**Isovalue/au**	**Volume/Å^3**	**Surface Area Å^2**	**% of Cell Volume**
	0.002	256.68	860.51	10.49%
	0.001	87.49	370.38	3.58%
	0.0005	15.42	92.03	0.63%
	0.0003	0.91	7.75	0.04%
Anhydrous Theophylline	**Isovalue/au**	**Volume/Å^3**	**Surface Area Å^2**	**% of Cell Volume**
	0.002	82.50	268.56	10.29%
	0.001	28.02	115.76	3.49%
	0.0005	6.01	34.77	0.75%
	0.0003	0.25	3.52	0.03%

Electrostatic Potential

The atomic charges for co-crystal (1) were calculated using the XDPROP utility of the XD package and AIMALL software[101]. The multipolar charge represents the valence shell electron population i.e., the total charge minus the core charge. The programs XDPROP and AIMALL were also used to calculate the charge and the atomic 'regions' identified by a local zero flux in the gradient vector field of the electron density.

Key differences in charge for co-crystal (**1**) are listed in Table 7. Bader charge values do not include ESDs since the XD package does not provide such calculation options. However, the integrated accuracy can be correlated to an average Lagrangian value of 7.35 x10^{-4} calculated from a TOPINT refinement for each atom within co-crystal (**1**). Differences highlighted between EXP and SP model Bader charges in (**1**) were noted at carbon atoms C(3') (0.2 e), C(3) (0.2 e), C(01) (0.3 e), and C(03') (0.3 e). This variation between models is attributed to crystal packing influences in the EXP model as these carbon atoms are all

involved directly in intermolecular hydrogen bonding. Atoms C(2) and N(3) also present with a difference in charge (0.4 e and -0.5 e respectively) but are not involved in intermolecular hydrogen bonding. In addition to the overall redistribution of charge due across the co-crystal, these atoms are influenced directly from the aromatic donor-acceptor interactions present in the triclinic form of co-crystal (**1**). This information is valuable to pharmaceutical companies to draw upon when designing or selecting future coformers. The redistribution of charge certainly is a pivotal key in the geometric formation of an enhanced co-crystalline structure when formulating. Anticipation of such effects derived from charge density data, coupled with physical formulation testing will optimise the time taken and fiscal investment on pharmaceutical development.

Table 7 – Selected Bader and Multipole atomic charges of interest within co-crystal (**1**). The full list is available with ESDs under Table S10 in the ESI.

THEOPHYLLINE1	**Bader Charge**		
Atoms	**SP Ω (e)**	**EXP Ω (e)**	**Difference (SP – EXP)**
C(1')	1.0	0.9	0.1
C(2')	1.0	0.7	0.3
C(3')	1.7	1.5	0.2
C(4')	1.2	1.1	0.1
N(1')	-1.4	-1.0	-0.4
N(2')	-1.2	-0.8	-0.4
N(3')	-1.4	-1.0	-0.4
N(4')	-0.9	-0.9	0.0
O(1')	-1.2	-1.0	-0.3
O(2')	-1.2	-0.9	-0.3

MALONICACID2	**Bader Charge**		
Atoms	**SP Ω (e)**	**EXP Ω (e)**	**Difference (SP – EXP)**
C(01')	1.6	1.4	0.2
C(03')	1.6	1.3	0.3
O(01')	-1.3	-1.2	-0.1

O(02')	-1.2	-1.0	-0.2
O(03')	-1.2	-1.0	-0.3
O(04')	-1.3	-1.1	-0.2

THEOPHYLLINE3	**Bader Charge**		
Atoms	**SP Ω (e)**	**EXP Ω (e)**	**Difference (SP – EXP)**
C(1)	1.0	0.8	0.2
C(2)	1.0	0.6	0.4
C(3)	1.7	1.5	0.2
C(4)	1.2	1.1	0.1
N(1)	-1.4	-1.1	-0.3
N(2)	-1.2	-0.8	-0.4
N(3)	-1.4	-0.9	-0.5
N(4)	-0.9	-0.9	0.0
O(1)	-1.2	-1.0	-0.2
O(2)	-1.2	-0.8	-0.4

MALONICACID4	**Bader Charge**		
Atoms	**SP Ω (e)**	**EXP Ω (e)**	**Difference (SP – EXP)**
C(01)	1.6	1.3	0.3
C(03)	1.6	1.4	0.2
O(01)	-1.2	-1.1	-0.1
O(02)	-1.2	-1.0	-0.2
O(03)	-1.2	-0.9	-0.3
O(04)	-1.2	-1.0	-0.2

The electronic charge difference is analysed further in Figure 15. The colour legend illustrates the charges at each atom in (**1**), with red denoting an electronegative and green/blue an electropositive region. As noted previously, carbonyl oxygen atoms involved intermolecular bonding outside of the chosen asymmetric unit exhibit a higher electronegativity than those which are bonded within (**1**). The charge distribution resulting from the intermolecular hydrogen bonding reflects the polar stabilisation noted previously in the shallower Laplacian gradients within the EXP model compared to the SP. Lai *et al.* [102] illustrated a similar redistribution of charge due to proton transfer. This resulted in stronger

hydrogen bonding intermolecularly and thus a higher stabilisation of the piroxicam polymorph studied. It is noticeable that the seven highest differences in Laplacian also exhibit the seven highest differences in atomic charge. These were identified as the carbonyl groups within the co-crystal (**1**). Of these, the top six exhibited bonding outside the asymmetric unit. The remainder were involved in bonding within the asymmetric unit. The reasoning for the top six exhibiting these differences is due to absence of hydrogen bonding within the gas phase model. Because of the missing crystal packing effects, it is postulated that this is the cause for the effect seen. The formula for defining an atomic basin is dictated by a zero flux in the gradient vector field [Equation 4][103].

$$\nabla\rho(\boldsymbol{r}).n(\boldsymbol{r}) = 0 \qquad (4)$$

A shift in the electron density due to intermolecular bonding and crystal field effects, results in an alteration of the gradient vector field between atomic boundaries. This redraws the atomic basin for each atom, which represents the differences seen in Table 7 across the Bader charges between the SP and EXP model. Therefore, electron density results such as these, are integral to the understanding of formulation and how it affects the redistribution of charge within a co-crystal.

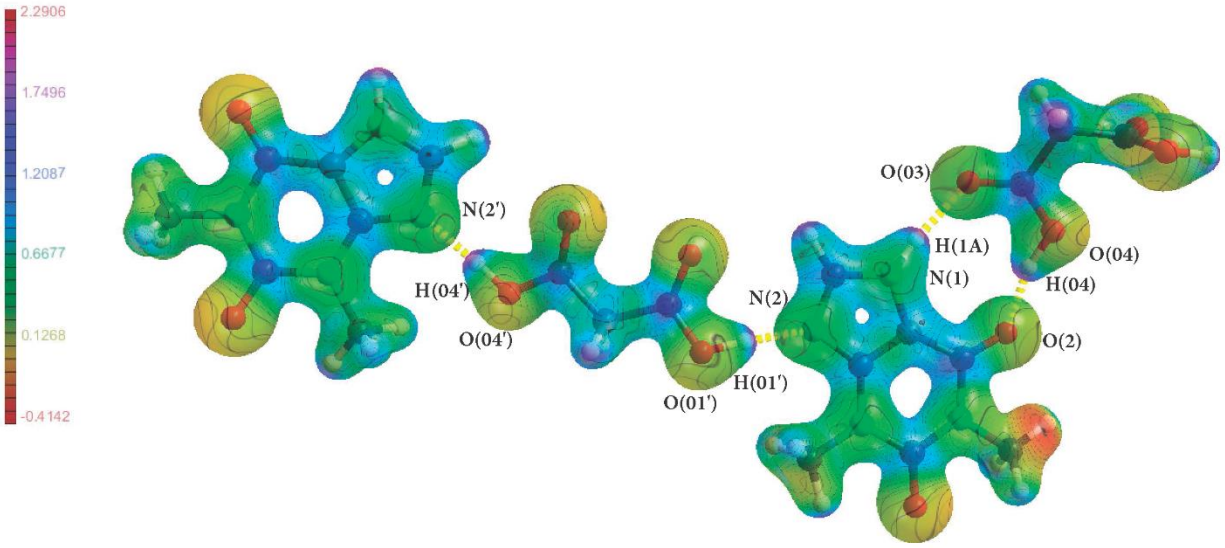

Figure 15 - Electrostatic potential of (**1**) mapped on the ρ isosurface

The application of such results to evaluation methods mentioned earlier such as dissolution tests, provides further advantages in streamlining the formulating process. These findings suggest the relative humidity influences on the formation of monohydrate theophylline will be reduced *via* co-crystallisation due to the reduced number of hydrogen bonding sites available. The number of hydrogen bond donor and acceptors utilised in the crystalline structure of theophylline anhydrate[99] is 2. Figure (8) shows the addition of malonic acid in co-crystal (**1**) utilises up to 8 hydrogen bond acceptor/donor sites. Trask *et al.* exhibited similar results across a range of carboxylic acid coformer combinations with theophylline.[51] The paper further identified the strength of the acid coformer was pivotal in the stability of the co-crystal. Oxalic acid was observed as the key coformer with theophylline in the experiment due to the highest protection from hydration with a significant relative humidity stability seen in the co-crystal compared to theophylline alone. Drawing from the charge influences seen by malonic acid above and the reduced carbon length present

in oxalic acid, the increased proximity of electronegative carboxyl groups suggests the increased effect observed.

Babu and Nangia identified the benefits of co-crystallisation seen in Remenar *et al*'s work on Itraconazole and tartaric acid.[104] The solubility was enhanced through the replication of a transitional, highly soluble amorphous state without the instability limitation usually accompanying it.[3] The dissociation of the coformer allows for the API to aggregate and form a disorganised higher free energy form.[105] Following Ostwald's Law of Stages [106], this high energy amorphous phase will transform to a metastable polymorph of the drug entailing a higher solubility before finally forming the most stable crystalline polymorph. The reference to the "spring and parachute" model described by Guzman *et al*. helped to illustrate this phase transition co-crystallised drugs go through upon dosing.[107] Lai *et al.*'s work on piroxicam polymorphic states identified differences in stabilisation via the correlation of lattice energy and dipole moment.[102]

These results are important as they included a monohydrated form in their study, which is a key real-world limitation with theophylline. The extended period of high solubility gives our co-crystal form (**1**) a greater potential to raise the bioavailability of its API theophylline, than the hydrated form it usually forms when stored on the shelf in a dispensary or when dosed individually.[108, 109]

Lattice Energy

In this study, the lattice energy of the individual components of the co-crystal (**1**) and the co-crystal itself were compared. The lattice energy reflects the energy needed to break down a crystalline structure into their individual units. In the case of co-crystals, we observe the dissociation of the active ingredient and the coformer. Comparison of co-crystals and their individual components in regard to lattice energy has been investigated in recent

times[110-112]. An accurate calculation of lattice energies is imperative for comparisons of crystals with co-crystals. A study by Spackman investigated the correlation between the sublimation enthalpy and lattice energy at room temperature for a number of co-crystal charge density studies[113]. The results provided an effective cross validation method for lattice energy calculations with the sublimation enthalpies of the studies crystals differing by no more than ~5 kJ mol^{-1}. The drawback of such a method is however, that the sublimation enthalpy for the molecular co-crystals must be available. As a novel co-crystal form, there is no sublimation enthalpy calculations for co-crystal **(1)**. In response to this hindrance, studies such as Thomas *et al.* investigated the confidence of using CE-B3LYP model energies when sublimation enthalpies were not known[114] . The study investigated 110 crystal lattice energies computed *via* CE-B3LYP and sublimation enthalpies and found a mean absolute percentage deviation in the range of 7-9%. The CE-B3LYP model energy calculation is available as tool within the CrystalExplorer software.

The lattice energy of (**1**) and the individual crystals were calculated using the CrystalExplorer software. This was done by calculating the energies between a central molecule and different molecules within a pre-set radius. For all systems, a radius of 25 angstroms was used and the calculations were carried out using the B3LYP functional and 6-31G(d,p) basis set [115]. The initial wavefunctions were calculated using the Gaussian 09 suite and pairwise interactions using CrystalExplorer. CrystalExplorer decomposes the total energy into four individual contributors: coulombic, polarisation, dispersion and repulsion forces. The total energy for each molecule is calculated as the sum of the four contributions with a scale factor applied. The scale factors for each energetic contribution was obtained by Mackenzie *et al.* based on comparing the results of the theoretical calculations with known experimental values [116]. The lattice energy was calculated using the method as described on the CrystalExplorer website[117]. The structure of theophylline was taken from the CSD:

CCDC 128707 [118] and malonic acid was accessed from the CSD: CCDC 1209218 [119]. Table 8 shows the total lattice energy and decomposed contributions for each system. The full table of scale corrected results for each molecule can be found under Tables S11-14 in the ESI.

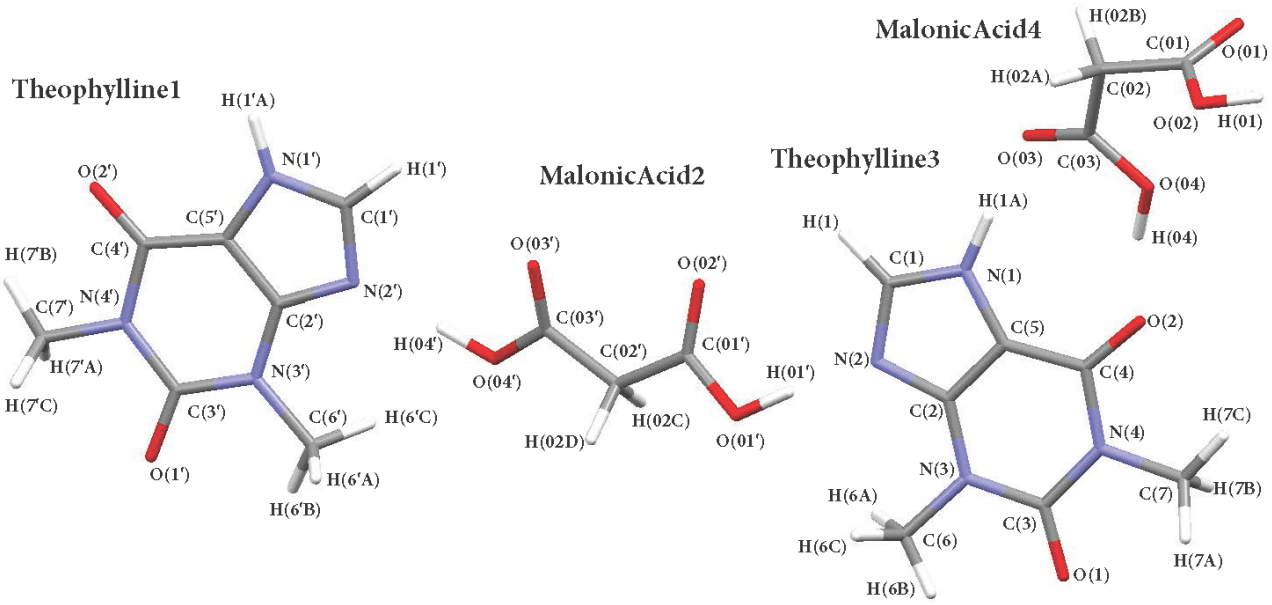

Figure 16 - Molecule identifiers used for co-crystal (**1**) in CrystalExplorer

Table 8 - Lattice energies calculated from CrystalExplorer for the triclinic co-crystal (**1**), the monoclinic theophylline malonic acid co-crystal and individual crystals of malonic acid and theophylline. The values were calculated using the method described on the CrystalExplorer website[117]. The correction factors for each contribution are: Coulombic – 1.057, Polarisation – 0.74, Dispersion – 0.871 and Repulsion – 0.618. All values listed are in kJ mol^{-1}.

Crystal	***Coulombic***	***Polarisation***	***Dispersion***	***Repulsion***	***Lattice***
*Co-Crystal **(1)***	-256.1	-26.2	-102.4	182.3	-101.6
Theophylline + Malonic	-212.1	-57.6	-165	273.3	-132.9

Acid Monoclinic [51]					
Malonic Acid [119]	-268.3	-67.9	-102.5	291.9	-126.5
Theophylline [118]	-89.2	-26.7	-114.8	121.6	-70

Table 8 illustrates a decrease in lattice energy for the theophylline co-crystal in the triclinic form (-101.6 kJmol^{-1}) as compared to the monoclinic form (-132.9 kJmol^{-1}). The lower lattice energy threshold provides a more rapid initiation of dissociation leading to the metastable polymorph stage formed as mentioned earlier. The distinguishing geometric differences between the polymorphs undoubtedly drive the difference between polymorphs in stabilisation through intermolecular bonds. A direct summation of individual components to compare to the total co-crystal lattice energy is restricted due to the geometric variation between individual molecules within the co-crystal such as the malonic acid rotation.

The aromatic donor-acceptor interactions mentioned earlier influence the atomic charge on atoms C(2) and N(3) [0.4 & -0.3 respectively]; which are not involved in any direct bonding. By applying methods developed by Waller *et al.* [120], the potential strength and contribution of these aromatic interactions on the molecule were also investigated. These values were calculated using the Gaussian 09 suite[61]. Individually the dimers above and below of the inclusive unit cell as seen previously in Figure 7, have a strength of -9.64 kJ mol^{-1} and -20.43 kJ mol^{-1} respectively (a total trimer value of -30.07 kJ mol^{-1}). The second dimer exhibited a higher potential due to the favoured orientation of the theophylline rings allowing for more interactions between the aromatic rings. The difference in distance between each ring sits in the region of 3.35-3.45 Å which is in agreement with the typical distances of π stacking.[121]

Lipinksi *et al.* [122] found the summation of crystal packing, cavitation and solvation energy to positively influence the overall aqueous solubility. As noted previously, the geometric orientation *via* co-crystallisation facilitates a definitive increase in the co-crystals surface bonding motifs through induced aromatic stacking. This is also seen in Overgaard *et al.*'s charge density study of aromatic amino acid metal complexes.[123] The increased stability between isomers of the co-crystal was concluded due to the increase in the number of aromatic donor-acceptor interactions. These enhanced chemical properties on total lattice energy translate to the real-world result where an API will exhibit both an increased solubility and stability.

The examination of correlation between charge density results and physical properties exhibited provides a significant lead compound prediction method before time and money are invested in the production process without a guaranteed return. It is noted however, that an inability to model entropy considerations accurately can reduce the overall solubility prediction.[124] Recent studies have made progress into the refinement of anisotropic displacement parameters that can help correlate the relationship between thermodynamic and physicochemical evaluation such as entropy and solubility[125]. Hoser & Madsen's refinement model will provide meaningful resources to future studies where physical testing results are on hand to correlate with diffraction data[126].

Conclusion

The experimental electron density distribution of a novel theophylline-malonic acid co-crystal system was determined via high resolution X-ray crystallography. The use of malonic acid stems from previous studies identifying successful co-operation between molecules; its toxicity profile would not support its application as a coformer for human

consumption in association with theophylline. Analysis of the charge distribution data was carried out and complemented with theoretical calculations. The redistribution of atomic charge within the co-crystal (**1**) and the numerous hydrogen bonding sites occupying the carbonyl groups explained the stabilisation of theophylline against hydration *via* co-crystallisation with malonic acid. The geometry of the co-crystal (**1**) favoured the addition of malonic acid, resulting in a geometric induced intermolecular bond via a trimer between overlapping theophylline molecules. The aromatic stacked trimers (-30.07 kJ mol^{-1}) between unit cells are not the only intermolecular bonds formed *via* co-crystallisation. Two strong reciprocal intermolecular malonic acid bridges are also formed *via* a hydrogen bond in each direction in and out of the unit cell between O(01)-H(01)···O(02) (-47.6 kJ mol^{-1} each individually). Favourable geometric formations found within the novel triclinic co-crystal (**1**) also reduced hygroscopicity with an increased promolecule density and reduced void space volume. The isolation of void spaces within the crystalline form is due to a combination of strong intermolecular bonding and a greater surface interaction distribution. This favourable isolation leads to a decrease in void volume of approximately 1% by the triclinic form over the monoclinic form. The stability of the triclinic theophylline co-crystal is further noted with a smaller lattice energy (-101.6 kJ mol^{-1}) than the more common monoclinic form (-132.9 kJ mol^{-1}). A lower lattice energy signifies a lower dissolution energy threshold which therefore speeds up the formation rate of a metastable polymorph upon dissociation when administered. Following the 'spring and parachute' theory, this in turn will increase the solubility of theophylline and potentially bioavailability. Utilising this information, along with the potential hydrogen bonding sites identified earlier, we can predict the physical property enhancements theoretically based on our experimental results for the co-crystal (**1**).

The explanation of theophylline's enhanced hygroscopic profile *via* co-crystallisation were identified through an ability to examine the redistributed charge density. Coupling such

results with physicochemical testing such as dissolution and solubility tests, can further enhance co-crystallisation studies resulting in stronger pharmaceutical development leads.

Supporting Information

†Electronic supplementary information (ESI) available. CCDC 2039707. For ESI and crystallographic data in CIF or other electronic formats, see DOI: XXXXXXX

The supporting information contains thermal diffuse scattering methods, crystallographic data, treatment and refinement methods, residual density analysis, topological findings, atomic charges and deformation density mapping.

Acknowledgments

The authors would like to acknowledge the Gadigal people of the Eora Nation as traditional custodians of the land upon where we work, and where this research was conducted. The authors would like to pay their respects those who have cared and continue to care for Country, to elders both past, present and emerging. S.A.S, F.L and B.A.H would like to thank The University of Sydney for our scholarships.

References

1. Elbagerma, M.; Edwards, H.; Munshi, T.; Hargreaves, M.; Matousek, P.; Scowen, I., Characterization of new cocrystals by Raman spectroscopy, powder X-ray diffraction, differential scanning calorimetry, and transmission Raman spectroscopy. *Crystal Growth & Design* **2010,** *10* (5), 2360-2371.
2. Almansa, C.; Merce, R.; Tesson, N.; Farran, J.; Tomàs, J.; Plata-Salaman, C. R., Co-Crystal of Tramadol hydrochloride–Celecoxib (CTC): a novel API–API co-crystal for the treatment of pain. *Crystal Growth & Design* **2017,** *17* (4), 1884-1892.
3. Babu, N. J.; Nangia, A., Solubility advantage of amorphous drugs and pharmaceutical cocrystals. *Crystal Growth & Design* **2011,** *11* (7), 2662-2679.
4. Chen, Y.; Li, L.; Yao, J.; Ma, Y.-Y.; Chen, J.-M.; Lu, T.-B., Improving the solubility and bioavailability of apixaban via apixaban–oxalic acid cocrystal. *Crystal Growth & Design* **2016,** *16* (5), 2923-2930.
5. Good, D. J.; Rodriguez-Hornedo, N., Solubility advantage of pharmaceutical cocrystals. *Crystal Growth and Design* **2009,** *9* (5), 2252-2264.

6. Goud, N. R.; Gangavaram, S.; Suresh, K.; Pal, S.; Manjunatha, S. G.; Nambiar, S.; Nangia, A., Novel furosemide cocrystals and selection of high solubility drug forms. *Journal of pharmaceutical sciences* **2012,** *101* (2), 664-680.
7. Huang, Y.; Zhang, B.; Gao, Y.; Zhang, J.; Shi, L., Baicalein–nicotinamide cocrystal with enhanced solubility, dissolution, and oral bioavailability. *Journal of pharmaceutical sciences* **2014,** *103* (8), 2330-2337.
8. Patole, T.; Deshpande, A., Co-Crystallization-A Technique for Solubility Enhancement. *International Journal of Pharmaceutical Sciences and Research* **2014,** *5* (9), 3566.
9. Smith, A. J.; Kavuru, P.; Wojtas, L.; Zaworotko, M. J.; Shytle, R. D., Cocrystals of quercetin with improved solubility and oral bioavailability. *Molecular pharmaceutics* **2011,** *8* (5), 1867-1876.
10. Sopyan, I.; Fudholi, A.; Muchtaridi, M.; Puspitasari, I., A Novel of Cocrystalization to Improve Solubility and Dissolution rate of Simvastatin. *International Journal of PharmTech Research* **2016,** *9* (6), 483-491.
11. Shan, N.; Zaworotko, M. J., The role of cocrystals in pharmaceutical science. *Drug discovery today* **2008,** *13* (9), 440-446.
12. Chennuru, R.; Devarapalli, R.; Rengaraj, P.; Srinivas, P.; Dey, S.; Reddy, C. M., Improving Solubility of Poorly Soluble Abiraterone Acetate by Co-Crystal Design aided by In-Silico Screening. *Crystal Growth & Design* **2020**.
13. Martin, F. A.; Pop, M. M.; Borodi, G.; Filip, X.; Kacso, I., Ketoconazole salt and co-crystals with enhanced aqueous solubility. *Crystal growth & design* **2013,** *13* (10), 4295-4304.
14. Serajuddin, A. T., Salt formation to improve drug solubility. *Advanced drug delivery reviews* **2007,** *59* (7), 603-616.
15. Hickey, M. B.; Peterson, M. L.; Scoppettuolo, L. A.; Morrisette, S. L.; Vetter, A.; Guzmán, H.; Remenar, J. F.; Zhang, Z.; Tawa, M. D.; Haley, S., Performance comparison of a co-crystal of carbamazepine with marketed product. *European journal of pharmaceutics and biopharmaceutics* **2007,** *67* (1), 112-119.
16. Surov, A. O.; Volkova, T. V.; Churakov, A. V.; Proshin, A. N.; Terekhova, I. V.; Perlovich, G. L., Cocrystal formation, crystal structure, solubility and permeability studies for novel 1, 2, 4-thiadiazole derivative as a potent neuroprotector. *European Journal of Pharmaceutical Sciences* **2017,** *109*, 31-39.
17. Sanphui, P.; Devi, V. K.; Clara, D.; Malviya, N.; Ganguly, S.; Desiraju, G. R., Cocrystals of hydrochlorothiazide: solubility and diffusion/permeability enhancements through drug–coformer interactions. *Molecular Pharmaceutics* **2015,** *12* (5), 1615-1622.
18. Bhatt, P. M.; Ravindra, N. V.; Banerjee, R.; Desiraju, G. R., Saccharin as a salt former. Enhanced solubilities of saccharinates of active pharmaceutical ingredients. *Chemical Communications* **2005,** (8), 1073-1075.
19. Haeria, A. N.; Ismail, I., Characterization and Dissolution Test of Aspirin-Nicotinamide Cocrystal. *substance* **2015,** *4* (5), 8-12.
20. Batisai, E.; Ayamine, A.; Kilinkissa, O. E.; Báthori, N. B., Melting point–solubility–structure correlations in multicomponent crystals containing fumaric or adipic acid. *CrystEngComm* **2014,** *16* (43), 9992-9998.
21. Katritzky, A. R.; Jain, R.; Lomaka, A.; Petrukhin, R.; Maran, U.; Karelson, M., Perspective on the relationship between melting points and chemical structure. *Crystal Growth & Design* **2001,** *1* (4), 261-265.
22. Chickos, J. S.; Nichols, G.; Ruelle, P., The estimation of melting points and fusion enthalpies using experimental solubilities, estimated total phase change entropies, and mobile

order and disorder theory. *Journal of chemical information and computer sciences* **2002,** *42* (2), 368-374.
23. Wenger, M.; Bernstein, J., An alternate crystal form of gabapentin: a cocrystal with oxalic acid. *Crystal Growth and Design* **2008,** *8* (5), 1595-1598.
24. Yadav, S.; Gupta, P. C.; Sharma, N.; Kumar, J., Cocrystals: An alternative approach to modify physicochemical properties of drugs. *International Journal of Pharmaceutical, Chemical & Biological Sciences* **2015,** *5* (2).
25. Martindale, W. H., The Extra Pharmacopoeia, vol. 1. *The Extra Pharmacopoeia, Vol. 1* **1936,** (Edn 21).
26. Hopkins, M. E.; MacKenzie-Ross, R. V., Case Report: The risks associated with chronic theophylline therapy and measures designed to improve monitoring and management. *BMC Pharmacology and Toxicology* **2016,** *17* (1), 13.
27. Kacirova, I.; Grundmann, M., TDM of Theophylline and Digoxin as an Indicator of the Quality of Medical Care: Results of The 7-Years Monitoring. *Clinical Therapeutics* **2017,** *39* (8), e83-e84.
28. Otsuka, M.; Kaneniwa, N.; Kawakami, K., Effect of surface characteristics of theophylline anhydrate powder on hygroscopic stability. *Journal of pharmacy and pharmacology* **1990,** *42* (9), 606-610.
29. Zhong, J.; Tang, N.; Asadzadeh, B.; Yan, W., Measurement and Correlation of Solubility of Theobromine, Theophylline, and Caffeine in Water and Organic Solvents at Various Temperatures. *Journal of Chemical & Engineering Data* **2017**.
30. Kemp, R. B., *Handbook of thermal analysis and calorimetry: from macromolecules to man*. Elsevier: 1999.
31. Fischer, F.; Schmidt, M. U.; Greiser, S.; Emmerling, F., The challenging case of the theophylline–benzamide cocrystal. *Acta Crystallographica Section C: Structural Chemistry* **2016,** *72* (3), 217-224.
32. Fulias, A.; Soica, C.; Ledeti, I.; Vlase, T.; Vlase, G.; Suta, L.-M.; Belu, I., Characterization of pharmaceutical acetylsalicylic acid—theophylline cocrystal obtained by slurry method under microwave irradiation. *Rev. Chim.-Buchar* **2014,** *65*, 1281-1284.
33. Lu, J.; Cruz-Cabeza, A. J.; Rohani, S.; Jennings, M. C., A 2: 1 sulfamethazine–theophylline cocrystal exhibiting two tautomers of sulfamethazine. *Acta Crystallographica Section C: Crystal Structure Communications* **2011,** *67* (8), o306-o309.
34. Wang, L.; Luo, M.; Li, J.; Wang, J.; Zhang, H.; Deng, Z., Sweet Theophylline Cocrystal with Two Tautomers of Acesulfame. *Crystal Growth & Design* **2015,** *15* (6), 2574-2578.
35. Ervasti, T.; Aaltonen, J.; Ketolainen, J., Theophylline–nicotinamide cocrystal formation in physical mixture during storage. *International journal of pharmaceutics* **2015,** *486* (1), 121-130.
36. Dittrich, B., Is there a future for topological analysis in experimental charge-density research? *Acta Crystallographica Section B: Structural Science, Crystal Engineering and Materials* **2017,** *73* (3), 325-329.
37. Macchi, P., The future of topological analysis in experimental charge-density research. *Acta Crystallographica Section B: Structural Science, Crystal Engineering and Materials* **2017,** *73* (3), 330-336.
38. Malińska, M.; Jarzembska, K. N.; Goral, A. M.; Kutner, A.; Woźniak, K.; Dominiak, P. M., Sunitinib: from charge-density studies to interaction with proteins. *Acta Crystallographica Section D: Biological Crystallography* **2014,** *70* (5), 1257-1270.
39. Gryl, M.; Cenedese, S.; Stadnicka, K., Crystal engineering and charge density study of pharmaceutical nonlinear optical material: melamine-barbital co-crystal. *The Journal of Physical Chemistry C* **2015,** *119* (1), 590-598.

40. Korlyukov, A. A.; Malinska, M.; Vologzhanina, A. V.; Goizman, M. S.; Trzybinski, D.; Wozniak, K., Charge density view on bicalutamide molecular interactions in the monoclinic polymorph and androgen receptor binding pocket. *IUCrJ* **2020,** *7* (1).
41. Korlyukov, A. A.; Vologzhanina, A. V.; Trzybinski, D.; Malinska, M.; Wozniak, K., Charge density analysis of abiraterone acetate. *Acta Crystallographica Section B: Structural Science, Crystal Engineering and Materials* **2020,** *76* (6).
42. Pawlędzio, S.; Makal, A.; Trzybiński, D.; Woźniak, K., Crystal structure, interaction energies and experimental electron density of the popular drug ketoprophen. *IUCrJ* **2018,** *5* (6), 841-853.
43. Wanat, M.; Malinska, M.; Kutner, A.; Wozniak, K., Effect of vitamin D conformation on interactions and packing in the crystal lattice. *Crystal Growth & Design* **2018,** *18* (6), 3385-3396.
44. Devi, R. N.; Stephen, A. D.; Justin, P.; Saravanan, K.; Macchi, P.; Jelsch, C., Topological and electrostatic properties of diclofenac molecule as a non-steroidal anti-inflammatory drug: An experimental and theoretical study. *Journal of Molecular Structure* **2019,** *1196*, 42-53.
45. Jelsch, C.; Bibila Mayaya Bisseyou, Y., Atom interaction propensities of oxygenated chemical functions in crystal packings. *IUCrJ* **2017,** *4* (2), 158-174.
46. Klai, K.; Soudani, S.; Jelsch, C.; Lefebvre, F.; Kaminsky, W.; Fujita, W.; Nasr, C. B.; Kaabi, K., Crystal structure, Hirshfeld surface analysis, and physicochemical studies of a new Cu (II) complex with 2-amino-4-methylpyrimidine. *Journal of Molecular Structure* **2019,** *1194*, 297-304.
47. Niranjana Devi, R.; Jelsch, C.; Israel, S.; Aubert, E.; Anzline, C.; Hosamani, A. A., Charge density analysis of metformin chloride, a biguanide anti-hyperglycemic agent. *Acta Crystallographica Section B: Structural Science, Crystal Engineering and Materials* **2017,** *73* (1), 10-22.
48. Rajendran, N. D.; Stephen, A. D.; Jelsch, C.; Escudero-Adán, E. C., Experimental Charge Density Analysis of the Anti-inflammatory Drug Meloxicam [sodium 4-hydroxy-2-methyl-/V-(5-methyl-1, 3-thiazol-2-yl)-1, 1-dioxo-1$ l^{6}, 2-benzothiazine-3-carboxamide Monohydrate]. *Croatica Chemica Acta* **2018,** *91* (2), 221-233.
49. Aitipamula, S.; Vangala, V. R., X-ray crystallography and its role in understanding the physicochemical properties of pharmaceutical cocrystals. *Journal of the Indian Institute of Science* **2017,** *97* (2), 227-243.
50. Ueda, H.; Muranushi, N.; Sakuma, S.; Ida, Y.; Endoh, T.; Kadota, K.; Tozuka, Y., A strategy for co-former selection to design stable co-amorphous formations based on physicochemical properties of non-steroidal inflammatory drugs. *Pharmaceutical research* **2016,** *33* (4), 1018-1029.
51. Trask, A. V.; Motherwell, W. S.; Jones, W., Physical stability enhancement of theophylline via cocrystallization. *International journal of pharmaceutics* **2006,** *320* (1), 114-123.
52. Oxford, D. *CrysAlis^{Pro}*, 1.171.37.31b; Oxford Diffraction Ltd: Abingdon, England, 2006.
53. Volkov, A.; Macchi, P.; Farrugia, L. J.; Gatti, C.; Mallinson, P.; Richter, T.; Koritsanszky, T. *XD2006- a computer program for multipole refinement, topological analysis of charge densities and evaluation of intermolecular energies from experimental or theoretical structure factors*, 2006.
54. Hansen, N. K.; Coppens, P., Electron population analysis of accurate diffraction data. VI. Testing aspherical atom refinements on small-molecule data sets. *Acta Crystallogr., Sect. A* **1978,** *A34* (6), 909-21.

55. Sheldrick, G. M., A short history of SHELX. *Acta Crystallogr., Sect. A: Found. Crystallogr.* **2008,** *64* (1), 112-122.
56. Allen, F. H.; Kennard, O.; Watson, D. G.; Brammer, L.; Orpen, A. G.; Taylor, R., Tables of bond lengths determined by x-ray and neutron diffraction. Part 1. Bond lengths in organic compounds. *J. Chem. Soc., Perkin Trans. 2* **1987,** (12), S1-S19.
57. Koritsanszky, T.; Mallinson, P.; Macchi, P.; Volkov, A.; Gatti, C.; Milano, C.-I.; Richter, T.; Farrugia, L., Manual Version February 2015 Program Version 6.03 February 2015.
58. Hirshfeld, F. L., Can x-ray data distinguish bonding effects from vibrational smearing? *Acta Crystallogr., Sect. A* **1976,** *A32, Pt. 2*, 239-44.
59. Hoser, A. A.; Dominiak, P. M.; Wozniak, K., Towards the best model for H atoms in experimental charge-density refinement. *Acta Crystallogr., Sect. A: Found. Crystallogr.* **2009,** *65* (4), 300-311.
60. Madsen, A. O., SHADE web server for estimation of hydrogen anisotropic displacement parameters. *J. Appl. Crystallogr.* **2006,** *39* (5), 757-758.
61. Frisch, M. J.; Trucks, G. W.; Schlegel, H. B.; Scuseria, G. E.; Robb, M. A.; Cheeseman, J. R.; Scalmani, G.; Barone, V.; Mennucci, B.; Petersson, G. A.; Nakatsuji, H.; Caricato, M.; Li, X.; Hratchian, H. P.; Izmaylov, A. F.; Bloino, J.; Zheng, G.; Sonnenberg, J. L.; Hada, M.; Ehara, M.; Toyota, K.; Fukuda, R.; Hasegawa, J.; Ishida, M.; Nakajima, T.; Honda, Y.; Kitao, O.; Nakai, H.; Vreven, T.; Montgomery, J. A., Jr.; Peralta, J. E.; Ogliaro, F.; Bearpark, M.; Heyd, J. J.; Brothers, E.; Kudin, K. N.; Staroverov, V. N.; Kobayashi, R.; Normand, J.; Raghavachari, K.; Rendell, A.; Burant, J. C.; Iyengar, S. S.; Tomasi, J.; Cossi, M.; Rega, N.; Millam, N. J.; Klene, M.; Knox, J. E.; Cross, J. B.; Bakken, V.; Adamo, C.; Jaramillo, J.; Gomperts, R.; Stratmann, R. E.; Yazyev, O.; Austin, A. J.; Cammi, R.; Pomelli, C.; Ochterski, J. W.; Martin, R. L.; Morokuma, K.; Zakrzewski, V. G.; Voth, G. A.; Salvador, P.; Dannenberg, J. J.; Dapprich, S.; Daniels, A. D.; Farkas, Ö.; Foresman, J. B.; Ortiz, J. V.; Cioslowski, J.; Fox, D. J. *Gaussian09*, 2006.
62. Becke, A. D., A new mixing of Hartree-Fock and local-density-functional theories. *J. Chem. Phys.* **1993,** *98* (2), 1372-7.
63. Lee, C.; Yang, W.; Parr, R. G., Development of the Colle-Salvetti correlation-energy formula into a functional of the electron density. *Phys. Rev. B: Condens. Matter* **1988,** *37* (2), 785-9.
64. Tawada, Y.; Tsuneda, T.; Yanagisawa, S.; Yanai, T.; Hirao, K., A long-range-corrected time-dependent density functional theory. *The Journal of chemical physics* **2004,** *120* (18), 8425-8433.
65. Yanai, T.; Tew, D. P.; Handy, N. C., A new hybrid exchange–correlation functional using the Coulomb-attenuating method (CAM-B3LYP). *Chemical Physics Letters* **2004,** *393* (1–3), 51-57.
66. Volkov, A.; Koritsanszky, T.; Chodkiewicz, M.; King, H. F., On the basis-set dependence of local and integrated electron density properties: Application of a new computer program for quantum-chemical density analysis. *Journal of computational chemistry* **2009,** *30* (9), 1379-1391.
67. Farrugia, L. J., ORTEP-3 for Windows-a version of ORTEP-III with a Graphical User Interface (GUI). *Journal of Applied Crystallography* **1997,** *30* (5), 565-565.
68. Bader, R. F., *Atoms in molecules*. Wiley Online Library: 1990.
69. Coppens, P., *X-ray charge densities and chemical bonding*. International Union of Crystallography: 1997; Vol. 4.
70. Hübschle, C. B.; Dittrich, B.; Grabowsky, S.; Messerschmidt, M.; Luger, P., Comparative experimental electron density and electron localization function study of

thymidine based on 20 K X-ray diffraction data. *Acta Crystallographica Section B: Structural Science* **2008,** *64* (3), 363-374.
71. Da'san MM, J.; Mebs, S.; Chęcińska, L.; Luger, P., Experimental charge density of sucrose at 20 K: bond topological, atomic, and intermolecular quantitative properties. *Carbohydrate research* **2007,** *342* (11), 1480-1489.
72. Hibbs, D. E.; Austin-Woods, C. J.; Platts, J. A.; Overgaard, J.; Turner, P., Experimental and theoretical charge density study of the neurotransmitter taurine. *Chemistry–A European Journal* **2003,** *9* (5), 1075-1084.
73. Du, J. J.; Váradi, L.; Tan, J.; Zhao, Y.; Groundwater, P. W.; Platts, J. A.; Hibbs, D. E., Experimental and theoretical charge density distribution in Pigment Yellow 101. *Phys. Chem. Chem. Phys.* **2015,** *17* (6), 4677-4686.
74. Munshi, P.; Guru Row, T. N., Intra-and intermolecular interactions in small bioactive molecules: cooperative features from experimental and theoretical charge-density analysis. *Acta Crystallographica Section B: Structural Science* **2006,** *62* (4), 612-626.
75. Bruno, I. J.; Cole, J. C.; Edgington, P. R.; Kessler, M.; Macrae, C. F.; McCabe, P.; Pearson, J.; Taylor, R., New software for searching the Cambridge Structural Database and visualizing crystal structures. *Acta Crystallographica Section B: Structural Science* **2002,** *58* (3), 389-397.
76. Chambers, J.; Migliorini, F. In *MERCURY-a new software package for orbital integrations*, AAS/Division for Planetary Sciences Meeting Abstracts# 29, 1997; p 27.06.
77. Cortés-Guzmán, F.; Gómez, R. M.; Rocha-Rinza, T.; Sánchez-Obregón, M. A.; Guevara-Vela, J. M., Valence Shell Charge Concentration (VSCC) Evolution: A Tool to Investigate the Transformations within a VSCC Throughout a Chemical Reaction. *The Journal of Physical Chemistry A* **2011,** *115* (45), 12924-12932.
78. Goedkoop, J.; MacGillavry, C., The crystal structure of malonic acid. *Acta Crystallographica* **1957,** *10* (2), 125-127.
79. Pimentel, G. C.; McClellan, A. L., The hydrogen bond. **1960**.
80. Taylor, R.; Kennard, O., Hydrogen-bond geometry in organic crystals. *Accounts of chemical research* **1984,** *17* (9), 320-326.
81. Wolff, S.; Grimwood, D.; McKinnon, J.; Jayatilaka, D.; Spackman, M., Crystal Explorer 2.0, University of Western Australia, Perth, Australia, 2007. *There is no corresponding record for this reference.[Google Scholar]*.
82. McKinnon, J. J.; Mitchell, A. S.; Spackman, M. A., Hirshfeld surfaces: a new tool for visualising and exploring molecular crystals. *Chemistry-A European Journal* **1998,** *4* (11), 2136-2141.
83. Spackman, M. A.; Jayatilaka, D., Hirshfeld surface analysis. *CrystEngComm* **2009,** *11* (1), 19-32.
84. McKinnon, J. J.; Jayatilaka, D.; Spackman, M. A., Towards quantitative analysis of intermolecular interactions with Hirshfeld surfaces. *Chemical Communications* **2007,** (37), 3814-3816.
85. Censi, R.; Di Martino, P., Polymorph impact on the bioavailability and stability of poorly soluble drugs. *Molecules* **2015,** *20* (10), 18759-18776.
86. Abboud, L., New prescription for drug makers: update the plants. *The Wall Street Journal Online* **2003**.
87. Spackman, M. A.; McKinnon, J. J., Fingerprinting intermolecular interactions in molecular crystals. *CrystEngComm* **2002,** *4* (66), 378-392.
88. Chourasia, M.; Sastry, G. M.; Sastry, G. N., Aromatic–Aromatic Interactions Database, A 2 ID: An analysis of aromatic π-networks in proteins. *International journal of biological macromolecules* **2011,** *48* (4), 540-552.

89. Martinez, C. R.; Iverson, B. L., Rethinking the term “pi-stacking”. *Chemical Science* **2012,** *3* (7), 2191-2201.
90. Matta, C. F.; Hernández-Trujillo, J.; Tang, T. H.; Bader, R. F., Hydrogen–hydrogen bonding: a stabilizing interaction in molecules and crystals. *Chemistry–A European Journal* **2003,** *9* (9), 1940-1951.
91. Grabowski, S. J., Ab Initio Calculations on Conventional and Unconventional Hydrogen BondsStudy of the Hydrogen Bond Strength. *The Journal of Physical Chemistry A* **2001,** *105* (47), 10739-10746.
92. Abramov, Y. A., On the possibility of kinetic energy density evaluation from the experimental electron-density distribution. *Acta Crystallographica Section A: Foundations of Crystallography* **1997,** *53* (3), 264-272.
93. Espinosa, E.; Molins, E.; Lecomte, C., Hydrogen bond strengths revealed by topological analyses of experimentally observed electron densities. *Chemical Physics Letters* **1998,** *285* (3), 170-173.
94. Aakeröy, C. B.; Seddon, K. R., The hydrogen bond and crystal engineering. *Chemical Society Reviews* **1993,** *22* (6), 397-407.
95. Jelsch, C.; Ejsmont, K.; Huder, L., The enrichment ratio of atomic contacts in crystals, an indicator derived from the Hirshfeld surface analysis. *IUCrJ* **2014,** *1* (2), 119-128.
96. Mitchell, A. S.; Spackman, M. A., Molecular surfaces from the promolecule: a comparison with Hartree–Fock ab initio electron density surfaces. *Journal of Computational Chemistry* **2000,** *21* (11), 933-942.
97. Turner, M. J.; McKinnon, J. J.; Jayatilaka, D.; Spackman, M. A., Visualisation and characterisation of voids in crystalline materials. *CrystEngComm* **2011,** *13* (6), 1804-1813.
98. Spek, A., The calculation of the solvent-accessible was performed by using the PLATON software (similarly hereinafter). *J. Appl. Crystallogr* **2003,** *36* (7).
99. Ebisuzaki, Y.; Boyle, P. D.; Smith, J. A., Methylxanthines. i. anhydrous theophylline. *Acta Crystallographica Section C: Crystal Structure Communications* **1997,** *53* (6), 777-779.
100. Soldatov, D. V.; Moudrakovski, I. L.; Grachev, E. V.; Ripmeester, J. A., Micropores in crystalline dipeptides as seen from the crystal structure, He pycnometry, and 129Xe NMR spectroscopy. *Journal of the American Chemical Society* **2006,** *128* (20), 6737-6744.
101. Keith, T. A. *AIMAll*, 14.06.21; TK Gristmill Software: Overland Park KS, USA, 2014.
102. Lai, F.; Du, J. J.; Williams, P. A.; Váradi, L.; Baker, D.; Groundwater, P. W.; Overgaard, J.; Platts, J. A.; Hibbs, D. E., A comparison of the experimental and theoretical charge density distributions in two polymorphic modifications of piroxicam. *Physical Chemistry Chemical Physics* **2016,** *18* (41), 28802-28818.
103. Bader, R. F., The zero-flux surface and the topological and quantum definitions of an atom in a molecule. *Theoretical chemistry accounts* **2001,** *105* (4), 276-283.
104. Remenar, J. F.; Morissette, S. L.; Peterson, M. L.; Moulton, B.; MacPhee, J. M.; Guzmán, H. R.; Almarsson, Ö., Crystal engineering of novel cocrystals of a triazole drug with 1, 4-dicarboxylic acids. *Journal of the American Chemical Society* **2003,** *125* (28), 8456-8457.
105. Kwei, G. Y.; Novak, L. B.; Hettrick, L. A.; Reiss, E. R.; Ostovic, D.; Loper, A. E.; Lui, C. Y.; Higgins, R. J.; Chen, I.-W.; Lin, J. H., Regiospecific intestinal absorption of the HIV protease inhibitor L-735,524 in beagle dogs. *Pharmaceutical research* **1995,** *12* (6), 884-888.
106. Threlfall, T., Structural and thermodynamic explanations of Ostwald's rule. *Organic process research & development* **2003,** *7* (6), 1017-1027.

107. Guzmán, H. R.; Tawa, M.; Zhang, Z.; Ratanabanangkoon, P.; Shaw, P.; Gardner, C. R.; Chen, H.; Moreau, J. P.; Almarsson, Ö.; Remenar, J. F., Combined use of crystalline salt forms and precipitation inhibitors to improve oral absorption of celecoxib from solid oral formulations. *Journal of pharmaceutical sciences* **2007,** *96* (10), 2686-2702.
108. Amado, A. M.; Nolasco, M. M.; Ribeiro-Claro, P. J., Probing pseudopolymorphic transitions in pharmaceutical solids using Raman spectroscopy: Hydration and dehydration of theophylline. *Journal of pharmaceutical sciences* **2007,** *96* (5), 1366-1379.
109. Sun, C.; Zhou, D.; Grant, D. J.; Young Jr, V. G., Theophylline monohydrate. *Acta Crystallographica Section E: Structure Reports Online* **2002,** *58* (4), o368-o370.
110. Habgood, M.; Deij, M. A.; Mazurek, J.; Price, S. L.; ter Horst, J. H., Carbamazepine co-crystallization with pyridine carboxamides: rationalization by complementary phase diagrams and crystal energy landscapes. *Crystal growth & design* **2010,** *10* (2), 903-912.
111. Chan, H. S.; Kendrick, J.; Neumann, M. A.; Leusen, F. J., Towards ab initio screening of co-crystal formation through lattice energy calculations and crystal structure prediction of nicotinamide, isonicotinamide, picolinamide and paracetamol multi-component crystals. *CrystEngComm* **2013,** *15* (19), 3799-3807.
112. Polito, M.; D'Oria, E.; Maini, L.; Karamertzanis, P. G.; Grepioni, F.; Braga, D.; Price, S. L., The crystal structures of chloro and methyl ortho-benzoic acids and their co-crystal: rationalizing similarities and differences. *CrystEngComm* **2008,** *10* (12), 1848-1854.
113. Spackman, M. A., Towards the use of experimental electron densities to estimate reliable lattice energies. *CrystEngComm* **2018,** *20* (36), 5340-5347.
114. Thomas, S. P.; Spackman, P. R.; Jayatilaka, D.; Spackman, M. A., Accurate lattice energies for molecular crystals from experimental crystal structures. *Journal of chemical theory and computation* **2018,** *14* (3), 1614-1623.
115. Gavezzotti, A., Calculation of intermolecular interaction energies by direct numerical integration over electron densities. 2. An improved polarization model and the evaluation of dispersion and repulsion energies. *The Journal of Physical Chemistry B* **2003,** *107* (10), 2344-2353.
116. Mackenzie, C. F.; Spackman, P. R.; Jayatilaka, D.; Spackman, M. A., CrystalExplorer model energies and energy frameworks: extension to metal coordination compounds, organic salts, solvates and open-shell systems. *IUCrJ* **2017,** *4* (5), 575-587.
117. Wiki, C. Lattice Energies. https://crystalexplorer.scb.uwa.edu.au/wiki/index.php/Lattice_Energies (accessed 11/12/2020).
118. Naqvi, A.; Bhattacharyya, G., Crystal data for anhydrous theophylline. *Journal of Applied Crystallography* **1981,** *14* (6), 464-464.
119. Jagannathan, N. R.; Rajan, S. S.; Subramanian, E., Refinement of the crystal structure of malonic acid, C3H4O4. *Journal of Chemical Crystallography* **1994,** *24* (1), 75-78.
120. Waller, M. P.; Robertazzi, A.; Platts, J. A.; Hibbs, D. E.; Williams, P. A., Hybrid density functional theory for π-stacking interactions: Application to benzenes, pyridines, and DNA bases. *Journal of computational chemistry* **2006,** *27* (4), 491-504.
121. Hunter, C. A.; Sanders, J. K., The nature of. pi.-. pi. interactions. *Journal of the American Chemical Society* **1990,** *112* (14), 5525-5534.
122. Lipinski, C. A.; Lombardo, F.; Dominy, B. W.; Feeney, P. J., Experimental and computational approaches to estimate solubility and permeability in drug discovery and development settings. *Advanced drug delivery reviews* **1997,** *23* (1-3), 3-25.
123. Overgaard, J.; Waller, M. P.; Piltz, R.; Platts, J. A.; Emseis, P.; Leverett, P.; Williams, P. A.; Hibbs, D. E., Experimental and theoretical charge density distribution in two ternary cobalt (III) complexes of aromatic amino acids. *The Journal of Physical Chemistry A* **2007,** *111* (40), 10123-10133.

124. Elder, D.; Holm, R., Aqueous solubility: simple predictive methods (in silico, in vitro and bio-relevant approaches). *International journal of pharmaceutics* **2013,** *453* (1), 3-11.
125. Madsen, A. Ø.; Larsen, S., Insight into Solid-State Entropy from Diffraction Data. *Angewandte Chemie International Edition* **2007,** *46* (45), 8609-8613.
126. Hoser, A. A.; Madsen, A. Ø., Dynamic quantum crystallography: lattice-dynamical models refined against diffraction data. I. Theory. *Acta Crystallographica Section A: Foundations and Advances* **2016,** *72* (2), 206-214.